LLNL-JRNL-810297

LAWRENCE
LIVERMORE
NATIONAL
LABORATORY

Two-Fluid and Kinetic Transport Physics of Kelvin-Helmholtz Instabilities in Nonuniform Low-Beta Plasmas

G. V. Vogman, J. H. Hammer, U. Shumlak, W. A. Farmer

May 15, 2020

Physics of Plasmas

Disclaimer

This document was prepared as an account of work sponsored by an agency of the United States government. Neither the United States government nor Lawrence Livermore National Security, LLC, nor any of their employees makes any warranty, expressed or implied, or assumes any legal liability or responsibility for the accuracy, completeness, or usefulness of any information, apparatus, product, or process disclosed, or represents that its use would not infringe privately owned rights. Reference herein to any specific commercial product, process, or service by trade name, trademark, manufacturer, or otherwise does not necessarily constitute or imply its endorsement, recommendation, or favoring by the United States government or Lawrence Livermore National Security, LLC. The views and opinions of authors expressed herein do not necessarily state or reflect those of the United States government or Lawrence Livermore National Security, LLC, and shall not be used for advertising or product endorsement purposes.

Two-fluid and kinetic transport physics of Kelvin-Helmholtz instabilities in nonuniform low-beta plasmas

G.V. Vogman,[1, a)] J.H. Hammer,[1] U. Shumlak,[2] and W.A. Farmer[1]

[1)] *Lawrence Livermore National Laboratory, Livermore, California 94550, USA*

[2)] *Aerospace and Energetics Research Program, University of Washington, Seattle, Washington 98195, USA*

(Dated: 28 October 2020)

Hall-magnetohydrodynamic (Hall-MHD) theory, two-fluid simulations, and kinetic simulations are used to investigate the cross-field transport properties of Kelvin-Helmholtz instabilities in nonuniform low-beta collisionless plasmas. Hall-MHD analysis shows how the linear properties of the instability are modified by density gradients and magnetization. High-order accurate two-fluid and kinetic simulations, with complete dynamics of finite-mass electrons and ions, are applied to a suite of parameter cases to systematically assess the effects of diamagnetic drift, magnetization, charge separation, and finite Larmor motion. Initialization of exact two-species kinetic equilibria facilitates the study of isolated physical effects and enables detailed cross-comparisons between two-fluid and kinetic simulations, including for cases where ion gyroradii are comparable to gradient scale lengths. For nonuniform plasmas with significant space charge, the results of two-fluid and kinetic simulations are found to disagree with Hall-MHD predictions. Kelvin-Helmholtz instability growth rates, per unit shear, are shown to be smaller when ion diamagnetic drift and $E \times B$ drift are parallel and larger when the two drifts are antiparallel. The effect is attributed to polarization drift in the shear layer, which leads to redistribution of charge, alters the electric field that drives plasma advection, and consequently modifies growth rates. Instability-induced mass transport for different parameters is characterized in terms of the flux across the shear layer and a simplified diffusion model. Distribution functions from kinetic simulations are shown to deviate substantially from Maxwellian reconstructions, indicating the importance of kinetic physics during the nonlinear phase of the instability.

---

[a] Corresponding author vogman1@llnl.gov

I. INTRODUCTION

Transport of plasma perpendicular to a background magnetic field is a widely-observed phenomenon. Magnetic confinement fusion concepts fundamentally rely on understanding and controlling cross-field transport, as do technologies like Hall thrusters, high-power magnetrons, and magnetically insulated transmission lines. In plasmas where the ratio of thermal pressure to magnetic pressure is much less than unity (i.e. low-beta plasmas) and where the mean free path is long compared to other scale lengths, cross-field transport properties can be governed by density gradients, finite Larmor motion, drifts, sheared flows, charge separation, and microturbulence. In such plasmas, gradient-driven instabilities are candidate mechanisms of cross-field transport. The Kelvin-Helmholtz (KH) instability, which is driven by velocity shear, is a well-known example.

Collisionless low-beta plasmas that are subject to anomalous cross-field transport and that have properties conducive to KH instabilities are characteristic of those found in pulsed power inertial confinement fusion experiments. Pulsed power technology relies on magnetically insulated transmission lines (MITLs) to deliver megaamps of current to a load – without high-voltage arcs. Despite magnetic insulation, plasmas produced at electrode surfaces in MITLs undergo as yet unexplained cross-field transport that results in parasitic currents[1–6] and leads to contaminant plasma impinging on the load[7,8], thereby undercutting the performance of pulsed power experiments[1,9]. The surface-produced plasmas feature large density and electric field gradients that result in sheared flows, which can drive KH instabilities and transport. The near-anode and near-cathode plasmas, as well as their associated electric field profiles, are shown schematically in Fig. 1.

Plasma conditions in the MITL vary considerably depending on the current pulse, the distance from the load, and distance from a given electrode surface. The hydrogen plasmas can have densities as high as 10^{18} cm^{-3} at the electrode surface,[1] whereas away from the electrodes densities as low as 10^{11} cm^{-3} have been inferred[10]. The potential drop across the centimeter-scale anode-cathode gap is typically several megavolts and magnetic fields can range from zero to more than 200 tesla over the course of a 100 ns current pulse[1]. While direct measurements of plasma conditions are limited,[1] characteristic conditions at a fixed distance from the load can be estimated. For a 200 tesla magnetic field, assuming a density of 2×10^{14} cm^{-3} and a temperature of 10 keV, the Knudsen number – defined

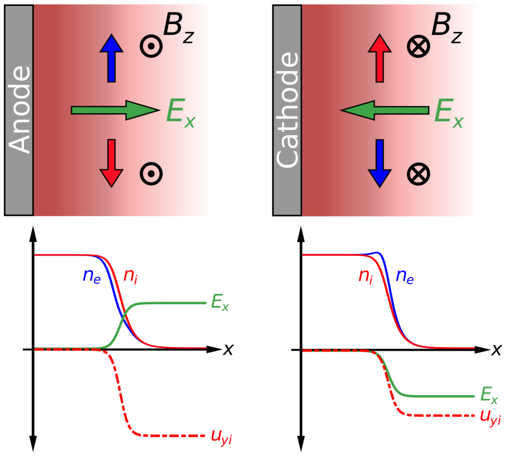

(a) (b)

FIG. 1: Schematic representation of (a) near-anode and (b) near-cathode plasmas that are produced at electrode surfaces in magnetically insulated transmission lines. Field orientation and profiles for the species number density, electric field, and ion velocity are shown separately for the two configurations. The direction of diamagnetic drift for ions and electrons (assuming uniform temperature) is indicated by red and blue arrows, respectively. In the anode configuration, the ion diamagnetic drift is in the same direction as the $E \times B$ drift.

here as the ratio of mean free path to the width of the anode-cathode gap – is on the order of 10^5 and the proton-proton collision frequency is seven orders of magnitude smaller than the proton cyclotron frequency. This means that collisions are expected to have a negligible effect on transport phenomena in this intermediate MITL environment. As shown in Fig. 1, the nonuniform plasmas are subject to $E \times B$ and diamagnetic drift, have non-zero space charge, and can feature ion gyroradii that are comparable to gradient scale lengths, such that their dynamics are governed by multi-fluid and kinetic physics. Significant space charge is expected since the configuration supports Brillouin-type flows.[11] Comprehensive investigation of KH-instability-driven cross-field transport in this complex setting requires high-fidelity modeling tools that can isolate the different physical effects.

In classical fluid theory and in plasmas, the energy source for the KH instability is the kinetic energy of relative motion of different fluid layers, such that for y-directed velocity with profile $u_y(x)$, larger velocity shear (du_y/dx) results in a greater tendency toward mixing and instability. A necessary condition for the instability is that the velocity profile must have an inflection point where $d^2u_y/dx^2 = 0$.[12] In order to fully capture growth rate dependence on perturbation wavenumber, the shear layer must have a finite gradient scale length[12,13]. For the magnetized plasmas of interest, where flow velocity is perpendicular to the magnetic field, the KH instability has been studied using ideal magnetohydrodynamic (MHD) models[14–19], more generalized single-fluid MHD models[20–22], quasineutral kinetic-fluid hybrid models[19,23,24], and kinetic models[18,19,25–31].

MHD models applied to uniform-density plasmas have shed light on the stabilizing role of in-plane magnetic fields and compressibility[14] and have been used to explore nonlinear properties like momentum transport, energy transport, and vortex coalescence[15,16,19,32]. Imposing infinitesimal gradient scale lengths for density and/or velocity, MHD models that incorporate finite Larmor radius (FLR) effects have shown that ion gyromotion in nonuniform-density plasmas can modify KH instability growth rates[20,21]. For uniform[26,27] or nearly-uniform[25] density profiles, kinetic theory analysis of KH instabilities has shown how FLR effects lead to reduced growth rates[25,27]. Kinetic simulations of nonuniform plasmas have shed light on mix[18] and on the properties of secondary instabilities in the presence of FLR effects[29]. Kinetic simulation studies have also explored how vorticity orientation relative to the magnetic field affects the development of the KH instability[19,29–31,33]. The degree to which KH instabilities – even those modeled using kinetic simulations – are influenced by two-fluid physics (e.g. charge separation, diamagnetic drift) as opposed to kinetic physics (e.g. FLR effects, non-Maxwellian distribution functions) remains unclear. Furthermore, in the presence of FLR effects, the use of fluid equilibria to initialize kinetic simulations[18,19,28–31,33] complicates the interpretation of kinetic simulation results[19,33,34] and makes it difficult to isolate single-fluid, multi-fluid, and kinetic physics.

To facilitate a more complete understanding of KH instabilities and associated cross-field transport in nonuniform collisionless low-beta plasmas, we conduct a systematic investigation based on Hall-MHD linear theory, two-fluid simulations, and kinetic simulations. By admitting finite gradient scale lengths for both velocity and density profiles, the Hall-MHD analysis shows how the linear properties of the instability are modified by density gradients, magnetization, and perturbation wavenumber. Detailed cross-comparisons between two-fluid and kinetic simulations are enabled by modeling complete dynamics of finite-mass electrons and ions and by initialization of self-consistent two-species kinetic equilibria, including for cases where ion gyroradii are comparable to gradient scale lengths[35]. These techniques, combined with the use of noise-free high-order accurate numerical methods, allow for systematic assessment of two-fluid and kinetic effects both in the linear and nonlinear phase of the KH instability. The findings demonstrate that diamagnetic drift and charge separation play an important role in the evolution of the instability, and further show how FLR effects and non-Maxwellian distribution functions modify the nonlinear dynamics.

This paper is organized as follows. Section II presents the Hall-MHD linear theory analysis for the KH instability in the presence of density gradients. Growth rates, oscillation frequencies, and associated eigenfunctions are presented and their dependence on magnetization, perturbation wavelength, and density profiles is characterized. Section III describes the governing equations and solvers used for two-fluid simulations and kinetic simulations, and presents the boundary conditions and the shear-layer equilibrium initial conditions for the nonuniform low-beta plasmas of interest. The procedure for setting up consistent initializations for two-fluid and kinetic simulations is described. Section IV presents results of two-fluid and kinetic simulations of KH instabilities in nonuniform plasmas. The linear phase of the evolution is compared to Hall-MHD theory and the role of diamagnetic drift, space charge, and finite Larmor radius effects are quantitatively assessed. The nonlinear phase of the KH instability is investigated for its non-adiabatic dynamics, its mass transport properties, and the degree to which velocity distribution functions deviate away from a Maxwellian. Section V presents concluding remarks.

II. HALL-MHD LINEAR THEORY ANALYSIS

To capture the properties of KH instabilities in low-beta plasmas with finite density gradients, we apply Hall-MHD theory, wherein the plasma is treated as isothermal, quasineutral, and electron inertia is assumed to be negligible. The magnetic field is assumed to be uniform and time-independent, such that magnetic fields generated by plasma currents are neglected. Since the magnetic moment is in effect constant, these assumptions are consistent with adiabatic theory for a 2D strongly-magnetized collisionless plasma. As is often justified for low-beta plasmas in a uniform magnetic field,[36,37] the electric field is treated as electrostatic, such that it can be expressed as the gradient of an electrostatic potential: $\boldsymbol{E} = -\nabla\phi$. Collisions and associated resistivity terms are neglected. The governing equations for a hydrogen plasma are thus

$$\frac{\partial n}{\partial t} + \nabla \cdot (n\boldsymbol{u}_i) = 0 \tag{1}$$

$$m_i n \frac{\partial \boldsymbol{u}_i}{\partial t} + m_i n \boldsymbol{u}_i \cdot \nabla \boldsymbol{u}_i + \nabla P_i - q_i n \left(-\nabla \phi + \boldsymbol{u}_i \times \boldsymbol{B}\right) = 0 \tag{2}$$

$$\nabla P_e - q_e n \left(-\nabla \phi + \boldsymbol{u}_e \times \boldsymbol{B}\right) = 0 \tag{3}$$

$$\nabla \cdot \sum_{s=e,i} q_s n_s \boldsymbol{u}_s = 0 \tag{4}$$

where $\boldsymbol{B}$ is the magnetic field, $q_i = -q_e = e$ is the particle charge, $n = n_i = n_e$ is the number density, m_i is the ion mass, $\boldsymbol{u}_s$ is the flow velocity, and P_s is the pressure for particle species s. The ideal gas law is used as the equation of state, such that $P_i = P_e = nT$, where $T = T_i = T_e$ is the temperature, which is assumed to be uniform. Equation (4) is a direct consequence of the quasineutrality approximation. Often in MHD analysis the ion momentum equation (Eq. (2)) and electron momentum equation (Eq. (3)) are combined, whereas here these equations are kept separate to facilitate the analysis of velocity profiles without having to specify currents. Because the ∇P_e term is retained, this model is sometimes referred to as "extended MHD".

A. Linear theory dispersion relation

The system of equations is linearized about an equilibrium in which the magnetic field $\boldsymbol{B}_0 = B_{z0}\hat{z}$ is uniform and the flow velocity for ions and electrons is along the y direction. The equilibrium species flow velocity $u_{s0y}(x)$, electrostatic potential $\phi_0(x)$, and number density $n_0(x)$ vary as a function of x and are independent of y. The equilibrium state is assumed to be independent of the z coordinate, such that dynamics are treated as being in the (x, y) plane. The equilibrium is perturbed with a wave vector $\boldsymbol{k} = k_y\hat{y}$. Expressing each variable in terms of an equilibrium quantity $\phi_0(x)$ plus a perturbation of the form

$\phi_1(x,y) = \hat{\phi}_1(x)e^{i(k_y y - \omega t)}$ and dropping nonlinear terms yields the linearized equations:

$$i\hat{n}_1(k_y u_{i0y} - \omega) + \frac{\partial}{\partial x}\left(n_0 \hat{u}_{i1x}\right) + ik_y n_0 \hat{u}_{i1y} = 0 \quad (5)$$

$$im_i n_0 \hat{u}_{i1x}(k_y u_{i0y} - \omega) - q_i \left[-\hat{n}_1 \frac{\partial \phi_0}{\partial x} - n_0 \frac{\partial \hat{\phi}_1}{\partial x} + n_0 \hat{u}_{i1y} B_{z0} + \hat{n}_1 u_{i0y} B_{z0}\right] + T\frac{\partial \hat{n}_1}{\partial x} = 0 \quad (6)$$

$$m_i n_0 \left[i\hat{u}_{i1y}(k_y u_{i0y} - \omega) + \hat{u}_{i1x}\frac{\partial u_{i0y}}{\partial x}\right] + q_i n_0 \left[ik_y \hat{\phi}_1 + \hat{u}_{i1x} B_{z0}\right] + ik_y \hat{n}_1 T = 0 \quad (7)$$

$$q_i \left[-n_0 \frac{\partial \hat{\phi}_1}{\partial x} + n_0 \hat{u}_{e1y} B_{z0} + \hat{n}_1 \left(u_{e0y} B_{z0} - \frac{\partial \phi_0}{\partial x}\right)\right] + T\frac{\partial \hat{n}_1}{\partial x} = 0 \quad (8)$$

$$-q_i n_0 \left[(ik_y)\hat{\phi}_1 + \hat{u}_{e1x} B_{z0}\right] + ik_y \hat{n}_1 T = 0 \quad (9)$$

$$\frac{\partial}{\partial x}\left[n_0(\hat{u}_{i1x} - \hat{u}_{e1x})\right] + ik_y n_0(\hat{u}_{i1y} - \hat{u}_{e1y}) + ik_y \hat{n}_1(u_{i0y} - u_{e0y}) = 0 \quad (10)$$

In the low-beta limit that is considered here, the plasma drift speed is much less than the Alfvén speed. Equations (5) to (10) combined with velocity from equilibrium force balance,

$$u_{i0y} = \left(\frac{1}{B_{z0}}\frac{\partial \phi_0}{\partial x} + \frac{T}{q_i B_{z0}}\frac{1}{n_0}\frac{\partial n_0}{\partial x}\right), \quad (11)$$

yield a second-order differential equation that encapsulates the eigenmode properties:

$$n_0 \hat{u}_{i1x} k_y^2 (k_y u_{i0y} - \omega) + \frac{\partial}{\partial x}\left[\frac{-(k_y u_{i0y} - \omega) n_0 \frac{\partial \hat{u}_{i1x}}{\partial x} + k_y \hat{u}_{i1x} n_0 \frac{\partial u_{i0y}}{\partial x}}{1 - \frac{1}{k_y \Omega_i}\frac{1}{n_0}\frac{\partial n_0}{\partial x}(k_y u_{i0y} - \omega)}\right] = 0, \quad (12)$$

where $\Omega_i = q_i B_{z0}/m_i$ is the ion cyclotron frequency, which has a positive sign, as is consistent with the assumed magnetic field orientation. Equation (12) indicates that magnetization, which is encapsulated in the ion cyclotron frequency, plays a role only if the equilibrium density gradient $\partial n_0/\partial x$ is non-zero. Equation (12) also relates the eigenfunction $\hat{u}_{i1x}$ to the equilibrium variables and to the perturbation wavenumber and frequency. In the limit of large magnetization ($\Omega_i \to \infty$) or zero density gradient, Eq. (12) reduces to the eigenmode equation obtained by Chandrasekhar from classical hydrodynamics theory[12]. Hydrodynamic analysis often includes a gravity (or gravity-like acceleration) term[12], which is not included in the present analysis, and which is not necessary to drive KH instabilities.

Consider a shear layer of half-width d in the center of a plasma bounded by impermeable walls at $x = \pm L$. As is standard practice in linear theory KH instability analysis[12], let the equilibrium velocity profile be piecewise linear with no variation outside of the shear layer, such that

$$u_{i0y}(x) = \begin{cases} V & x \in [-L, -d] \\ -\frac{V}{d}x & x \in [-d, d] \\ -V & x \in [d, L] \end{cases} . \tag{13}$$

Let the equilibrium number density profile be piecewise exponential with no variation inside the shear layer, such that

$$n_0(x) = \begin{cases} e^{a(x+d)} & x \in [-L, -d] \\ 1 & x \in [-d, d] \\ e^{b(x-d)} & x \in [d, L] \end{cases} . \tag{14}$$

Note that Eq. (14) can be rescaled by a constant and the following analysis would remain unchanged. The density profile is chosen to have a constant value of $\nabla n_0 / n_0$ on either side of the shear layer, such that

$$\frac{1}{n_0}\frac{\partial n_0}{\partial x} = \begin{cases} a & x \in [-L, -d] \\ 0 & x \in [-d, d] \\ b & x \in [d, L] \end{cases} . \tag{15}$$

Figure 2 shows the velocity profile of Eq. (13) and the density profile of Eq. (14) for $a = 0$ and $b < 0$. While in Eq. (14) we have chosen density to be continuous, discontinuous density profiles are also admissible. Density profiles that satisfy Eq. (15) admit analytic solutions for Eq. (12) and, unlike piecewise constant density profiles used in Refs. 17, 20, and 21, admit analysis of configurations with finite diamagnetic drift. Note that for this choice of density profile the velocity shear in the $x \in [-d, d]$ region is entirely due to $E \times B$ drift.

For the velocity and density profiles given by Eqs. (13) and (14), the eigenmode equation given by Eq. (12) can be solved for $\hat{u}_{i1x}$ and the associated dispersion relation that relates ω and k_y can be obtained – see Appendix A. Here we consider the special case where $a = 0$, such that the density profile is in effect

$$n_0(x) = \begin{cases} 1 & x \in [-L, d] \\ e^{b(x-d)} & x \in [d, L] \end{cases} \tag{16}$$

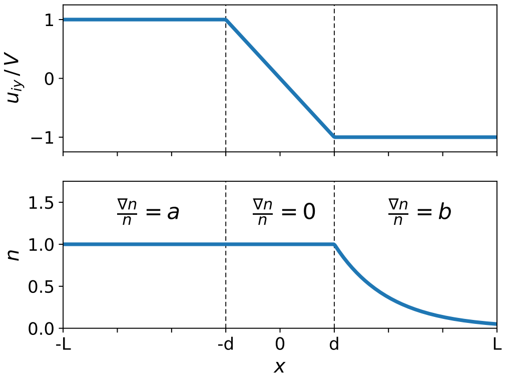

FIG. 2: Equilibrium profiles for a piecewise linear shear layer: ion velocity (top) and an example of a number density profile with $a = 0$ and $b < 0$ that satisfies Eq. (15) (bottom). These profiles admit analytic solutions for the eigenmode equation given in Eq. (12). For analytic solutions to exist, the value of $\nabla n/n$ should be constant outside of the shear layer and zero inside the shear layer.

and the solution to the eigenmode equation is

$$\hat{u}_{i1x} = \begin{cases} R_0 e^{k_y x} + S_0 e^{-k_y x} & x \in [-L, d] \\ R_b \exp\left(\left\{-\frac{b}{2} - \frac{1}{2}\sqrt{b^2 + 4k_y^2 \mathcal{B}}\right\} x\right) + S_b \exp\left(\left\{-\frac{b}{2} + \frac{1}{2}\sqrt{b^2 + 4k_y^2 \mathcal{B}}\right\} x\right) & x \in [d, L] \end{cases} \tag{17}$$

$$\mathcal{B} = \left(1 + \frac{b}{\Omega_i k_y}(k_y V + \omega)\right). \tag{18}$$

where $\{R_0, S_0, R_b, S_b\}$ are constant coefficients, which can be reduced to a single coefficient by applying $\hat{u}_{i1x} = 0$ boundary conditions at $x = \pm L$ and a continuity condition at $x = d$. The associated dispersion relation, the dimensional form of which is derived in Appendix A, is nondimensionalized such that spatial scales are normalized to the shear layer half-width d and temporal scales are normalized to the shear $\omega_s = V/d$, which is taken to be positive. The resulting closed-form nonlocal dispersion relation is

$$e^{-4\kappa}\left(\frac{\coth\left((\tilde{L}-1)\kappa\right) - 1 - \frac{1}{(\kappa-\tilde{\omega})}}{\coth\left((\tilde{L}-1)\kappa\right) + 1 - \frac{1}{(\kappa-\tilde{\omega})}}\right) = \frac{\left(\frac{\tilde{b}}{2} + \frac{1}{2}\sqrt{\tilde{b}^2 + 4\kappa^2\tilde{\mathcal{B}}}\coth\left(\frac{(\tilde{L}-1)}{2}\sqrt{\tilde{b}^2 + 4\kappa^2\tilde{\mathcal{B}}}\right) + \kappa\left(1 - \frac{1}{(\kappa+\tilde{\omega})}\right)\tilde{\mathcal{B}}\right)}{\left(\frac{\tilde{b}}{2} + \frac{1}{2}\sqrt{\tilde{b}^2 + 4\kappa^2\tilde{\mathcal{B}}}\coth\left(\frac{(\tilde{L}-1)}{2}\sqrt{\tilde{b}^2 + 4\kappa^2\tilde{\mathcal{B}}}\right) - \kappa\left(1 + \frac{1}{(\kappa+\tilde{\omega})}\right)\tilde{\mathcal{B}}\right)}, \tag{19}$$

where we have introduced the nondimensional parameters

$$\begin{aligned}
\kappa &= k_y d \\
\tilde{L} &= L/d \\
\tilde{\omega} &= \omega/\omega_s \\
\tilde{b} &= bd \\
\tilde{\mathcal{B}} &= 1 + \frac{\tilde{b}}{\tilde{\Omega}_i \kappa}(\kappa + \tilde{\omega}) \\
\tilde{\Omega}_i &= \Omega_i/\omega_s.
\end{aligned}$$

In addition to the classical features of the KH instability, Eq. (19) encapsulates the effects of diamagnetic drift and wall proximity. Diamagnetic drift is related to the term $\tilde{b}/\tilde{\Omega}_i$, which accounts for finite density gradients and magnetization – features that were not considered in previous MHD theoretical analyses[14,17,20,21]. This term drops out entirely if $\tilde{b} = 0$, such that the effect of magnetization only appears in the dispersion relation if the number density has a finite gradient. This feature of the dispersion relation is consistent with incompressible MHD linear theory analysis of the KH instability for a piecewise-uniform density configuration, wherein magnetic field terms drop out of the dispersion relation, independent of the choice of Ohm's law[17]. For fixed values of $\{\kappa, \tilde{L}, \tilde{b}, \tilde{\Omega}_i\}$ the dispersion relation in Eq. (19) can be solved numerically for $\tilde{\omega}$.

B. Growth rates and eigenfunctions

Some effects of density variation on growth rate can be examined in the classical fluid limit. In the absence of diamagnetic effects, various incompressible hydrodynamic limits of the dispersion relation can be obtained by taking the limit $\Omega_i \to \infty$ and explicitly solving for $\tilde{\omega}$. See Appendix B for details. For an infinite domain and $\tilde{b} = 0$, instability growth occurs for $\kappa \in [0, 0.639]$ with maximum growth rate 0.201 at $\kappa = 0.398$. Finite $\tilde{L}$ has a stabilizing effect. For an infinite domain and steep fall-off of density outside the shear layer, i.e. for $\tilde{L} \to \infty, \tilde{b} \to -\infty$, instability occurs for $\kappa \in [0, 0.916]$ with maximum growth rate 0.247 at $\kappa = 0.613$. For $\tilde{b} \to \infty$, the configuration is stable. Thus a density profile that decreases away from the shear layer results in a more unstable configuration as compared to the case of a uniform density profile. This is because the KH instability, which is driven by inertia, is easier to excite when the shear layer has a “free boundary”. Analogously, a density profile that increases away from the shear layer has a stabilizing effect, due to the larger inertia of the fluid outside of the shear layer.

To illustrate how plasma magnetization and finite density gradients affect the KH instability, the dispersion relation in Eq. (19) is solved for $\tilde{\omega}$ using the Newton method. For simplicity we set $\tilde{L} = 10$, which ensures that wall boundaries are sufficiently far from the shear layer so as to have a negligible effect. In general, $\tilde{\omega}$ has both a real and imaginary component, such that $\tilde{\omega} = \tilde{\omega}_R + i\tilde{\omega}_I$. The resulting growth rates, $\tilde{\omega}_I$, are plotted in Fig. 3 as a function of κ and $\tilde{b}$ for different levels of magnetization, which is set by the value of nondimensional ion cyclotron frequency $\tilde{\Omega}_i$.

For $\tilde{\Omega}_i \lesssim 1$, the dispersion relation exhibits high-wavenumber unstable modes, which appear as banded structures in the growth rate contour plot in Fig. 3(a). These banded structures can be explained by the coupling between the KH instability and drift waves. Coupling occurs when the Doppler-shifted frequency is equal to the drift wave frequency $\tilde{\omega}_D$, such that

$$\tilde{\omega}_R - \kappa \tilde{u}_{iy0}(x) = \tilde{\omega}_D, \tag{20}$$

where $\tilde{u}_{iy0}(x) = \frac{u_{iy0}(x)}{V}$ is the spatially-dependent nondimensional equilibrium ion velocity profile with range $[-1, 1]$. In the limit where $\left|\frac{\tilde{\omega}}{\tilde{\Omega}_i}\frac{\tilde{b}}{\kappa}\right| \gg 1$, the drift wave frequency is $\tilde{\omega}_D = \left(\frac{\kappa}{\tilde{b}} - 1\right)\tilde{\Omega}_i \approx -\tilde{\Omega}_i$, which is obtained by solving Eq. (12) and the associated dispersion relation for the case where n_0 is given by Eq. (16) and $u_{i0y} = 0$. Electrostatic drift waves with similar dispersion relations are described in Refs. 38–42. While high-wavenumber modes are not explored in detail here, it is worth noting that similar high-wavenumber unstable modes have been found in previous studies of magnetized shear layers, including in cold-fluid theoretical analysis of the diocotron instability in electron beams[43], nonlocal electrostatic kinetic theory analysis accounting for first order finite Larmor radius effects in plasma shear layers[25], and local electrostatic kinetic theory analysis of ion velocity shear instabilities[26]. MHD analysis that incorporates large effective Larmor radius physics has also demonstrated the existence of short-wavelength branches of the KH instability[20] for the case of discontinuous-step density profiles. In each of these studies, the high-wavenumber mode exhibits significantly smaller growth rates when compared to the classical KH mode – as is consistent with the trends in Fig. 3(a).

For sufficiently large magnetization, i.e. for $\tilde{\Omega}_i \gtrsim 1$: as $\tilde{b}$ decreases, the growth rate of the KH instability increases, the wavenumber associated with the peak growth rate increases, and the largest wavenumber that admits instability increases. This general trend is consistent with the hydrodynamic limits of the dispersion relation. In fact, in the limit $\tilde{\Omega}_i \to \infty$, the variation of growth rate with $\tilde{b}$ is largely a result of fluid inertia, such that the local average density matters more than the gradient of the density. This can be verified by deriving a dispersion relation for a piecewise-uniform equilibrium density profile with number density n_1 for $x < d$ and number density n_2 for $x \geq d$ (in this case $\tilde{\Omega}_i$ drops out of the dispersion relation), in which case the growth rate dependence on the ratio $n_2/n_1 \in [0, \infty)$ exhibits similar features to the growth rate dependence on $\tilde{b} \in (-\infty, \infty)$. Increasing magnetization tends to increase the range of unstable wavenumbers for $\tilde{b} < 0$ and decrease the range of unstable wavenumbers for $\tilde{b} > 0$. Overall, however, for $\tilde{\Omega}_i \gtrsim 1$ the effect of magnetization on growth rate is generally weak, as evidenced by the similarity of growth rates for the case where $\tilde{\Omega}_i = 2$ and the case where $\tilde{\Omega}_i \to \infty$, shown in Fig. 3(b) and Fig. 3(c), respectively.

The spatial structure of the eigenmode for the linear phase of instability development further elucidates the role of finite density gradients near the shear layer. The perturbed velocity eigenfunction $u_{i1x}(x, y) = \mathtt{Re}\left(\hat{u}_{i1x}(x) e^{ik_y y}\right)$ with $\hat{u}_{i1x}$ given in Eq. (17) and with $\tilde{L} = 10$ and $\kappa = 0.4$, is plotted in Fig. 4 for two density configurations. Figure 4 also shows the perturbed velocity vector field (u_{i1x}, u_{i1y}) and identifies the mixed-complex frequency for each configuration. For the uniform density configuration with $\tilde{b} = 0$ and $\tilde{\Omega}_i \neq 0$, which corresponds to the classical incompressible hydrodynamic limit, the largest amplitude features in u_{i1x} are at the edges of the shear layer. The features have a skew, such that extrema on the left side of the shear layer are offset in y from the extrema on the right side of the shear layer. See Fig. 4(a). The eigenmode structure is also characterized by circulation features in the velocity field at the edges of the shear layer – these ultimately lead to the formation of an eddy in the nonlinear phase of the KH instability. Introduction of density variation to right of the shear layer modifies the eigenmode structure, as shown in Fig. 4(b). In the nonuniform density configuration with $\tilde{b} = -1$ and $\tilde{\Omega}_i = 2$, the magnitude of the perturbed velocity u_{i1x} is largest at the right edge of the shear layer. In this case the extrema at the left and right edge of the shear layer exhibit a slightly larger offset in y and a larger region of the domain – primarily the low density region – is affected by the instability. It is worth noting that density variation outside of the shear layer introduces a

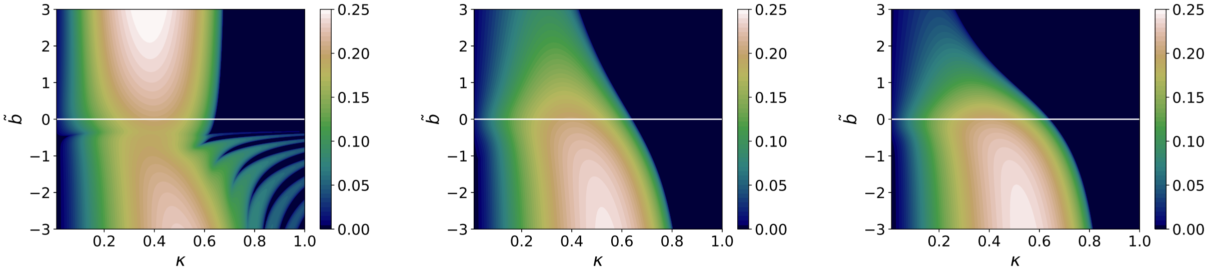

(a) $\tilde{\Omega}_i = 0.5$ (b) $\tilde{\Omega}_i = 2.0$ (c) $\tilde{\Omega}_i \to \infty$

FIG. 3: Instability growth rate $\tilde{\omega}_I$ obtained by solving the dispersion relation in Eq. (19) for different levels of magnetization: (a) $\tilde{\Omega}_i = 0.5$, (b) $\tilde{\Omega}_i = 2.0$, and (c) $\tilde{\Omega}_i \to \infty$. For all cases, $\tilde{L} = 10$. The growth rate is plotted as a function of nondimensional wavenumber $\kappa = k_y d$ and nondimensional parameter $\tilde{b} = bd$, which encapsulates the density gradient scale length to the right of the shear layer. For $\tilde{b} = 0$, denoted by the white horizontal lines, the plasma density is uniform, the instability is essentially hydrodynamic, and the growth rate is independent of $\tilde{\Omega}_i$. As the nondimensional ion cyclotron frequency $\tilde{\Omega}_i$ decreases, the parameter space over which an instability is admissible is modified. In addition to low wavenumber modes that are characteristic of the classical KH instability, high wavenumber unstable modes exist for $\tilde{\Omega}_i \lesssim 1$.

non-zero oscillation frequency, such that $\tilde{\omega}_R \neq 0$.

Taken together, the Hall-MHD-based eigenfunction and eigenvalue analysis shows how density gradients and magnetization affect the linear phase of the KH instability. For sufficiently low levels of magnetization, density variation can introduce high-wavenumber unstable modes. At high magnetization, where ion cyclotron frequency exceeds the velocity shear, plasma configurations where the density profile decreases away from the shear layer tend to be more unstable with the low density region more strongly affected by the KH instability.

III. SIMULATION SOLVERS AND EQUILIBRIUM SETUP

The linear theory analysis in Sec. II provides a basis for the study of more generalized physics and transport properties of KH instabilities in nonuniform low-beta collisionless plasmas. To investigate KH instability physics beyond the scope of the Hall-MHD description

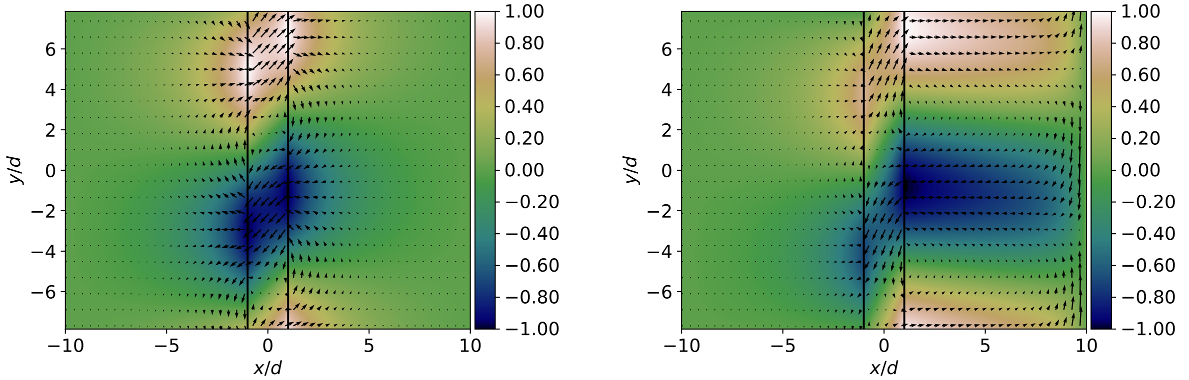

(a) $\tilde{\Omega}_i \neq 0, \tilde{b} = 0, \tilde{\omega} = i0.201$

(b) $\tilde{\Omega}_i = 2, \tilde{b} = -1, \tilde{\omega} = 0.091 + i0.222$

FIG. 4: The linear perturbed velocity $u_{ix1}(x, y)$ plotted in arbitrary units for two different configurations: (a) $\tilde{\Omega}_i \neq 0, \tilde{b} = 0$ for which $\tilde{\omega} = i0.201$; and (b) $\tilde{\Omega}_i = 2, \tilde{b} = -1$ for which $\tilde{\omega} = 0.091 + i0.222$. The perturbed velocity is obtained from the real part of the eigenfunction $\hat{u}_{ix1}(x)e^{ik_y y}$ with $\hat{u}_{ix1}$ given in Eq. (17) and with $\tilde{L} = 10$, $\kappa = 0.4$. Black arrows indicate the perturbed velocity magnitude and direction and vertical black lines denotes the edges of the shear layer. For the uniform density configuration with $\tilde{b} = 0$, corresponding to the incompressible uniform-density hydrodynamic KH instability, the perturbed velocity exhibits features of equal magnitude at both edges of the shear layer. Introducing finite density variation with $\tilde{b} = -1$ modifies the eigenmode structure such that the largest x-directed perturbed velocity is at the right edge of the shear layer and a larger region of the domain is affected by the instability.

we apply electromagnetic two-fluid simulations and two-species electrostatic kinetic simulations. Two-fluid simulations facilitate the self-consistent study of charge separation and diamagnetic drift in the shear layer, and kinetic simulations further enable the study of finite Larmor radius effects and associated non-Maxwellian distribution functions. Initial conditions for simulations are informed by the MITL application – the plasma configuration is shown schematically in Fig. 1. As before, we consider low-beta two-species – electron and ion – plasmas in the (x, y) plane with an out-of-plane magnetic field in the z direction and equilibrium flow velocity with contributions from $E \times B$ and diamagnetic drift.

A. Electromagnetic two-fluid simulations

1. *Governing equations and solver*

Two-fluid simulations use the nondimensional multi-fluid plasma model[44] as a basis. The multi-fluid model is described by the following governing equations for each species s:

$$\frac{\partial n_s}{\partial t} + \nabla \cdot (n_s \boldsymbol{u}_s) = 0 \tag{21}$$

$$\frac{\partial (n_s \boldsymbol{u}_s)}{\partial t} + \nabla \cdot (n_s \boldsymbol{u}_s \boldsymbol{u}_s) + \frac{1}{M_s} \nabla P_s = \frac{Z_s}{M_s} n_s \left(\boldsymbol{E} + \left(\frac{\Omega_p}{\omega_{pp}} \right) \boldsymbol{u}_s \times \boldsymbol{B} \right) \tag{22}$$

$$\frac{\partial \varepsilon_s}{\partial t} + \nabla \cdot ((\varepsilon_s + P_s) \boldsymbol{u}_s) = Z_s n_s \boldsymbol{u}_s \cdot \boldsymbol{E} \tag{23}$$

where

$$\varepsilon_s = \frac{1}{\gamma - 1} P_s + \frac{1}{2} M_s n_s u_s^2 \tag{24}$$

is the total energy of species s and $\gamma = (D_f + 2)/D_f$ is the adiabatic index, where D_f is the number of degrees of freedom. Unless otherwise noted, $D_f = 3$ such that $\gamma = 5/3$. Maxwell's equations, which describe the evolution of the electromagnetic fields are

$$-\left(\frac{\Omega_p}{\omega_{pp}} \right) \frac{\partial \boldsymbol{E}}{\partial t} + \nabla \times \boldsymbol{B} = \left(\frac{\Omega_p}{\omega_{pp}} \right) \sum_s Z_s n_s \boldsymbol{u}_s \tag{25}$$

$$\left(\frac{\Omega_p}{\omega_{pp}} \right) \frac{\partial \boldsymbol{B}}{\partial t} + \nabla \times \boldsymbol{E} = 0 \tag{26}$$

$$\nabla \cdot \boldsymbol{E} = \sum_s Z_s n_s \tag{27}$$

$$\nabla \cdot \boldsymbol{B} = 0 \tag{28}$$

Here n_s is the number density and $\boldsymbol{u}_s$ is the velocity of the fluid of species s, $\boldsymbol{B}$ is the magnetic field, $\boldsymbol{E}$ is the electric field, M_s is the ratio of particle mass to the proton mass, Z_s is the ratio of particle charge to the magnitude of the electron charge e, and Ω_p is the proton cyclotron frequency. In Eqs. (21) to (28) time is normalized to the proton plasma frequency ω_{pp}, velocity is normalized to the proton Alfvén speed v_A – defined in terms of a characteristic magnetic field B_0, and the electric field is normalized to the product $v_A B_0$. In effect, the characteristic length scale is $L_0 = v_A/\omega_{pp} = \delta_p \Omega_p/\omega_{pp}$, where δ_p is the proton skin depth. The normalization is described in Ref. 45. The equation of state, i.e. the closure model, is chosen to be the ideal gas law such that $P_s = n_s T_s$.

Assuming the plasma consists of protons and electrons, such that $Z_i = -Z_e = 1$, the multi-fluid model reduces to a two-fluid model. The two-fluid model retains electron inertia terms, does not invoke the quasineutrality approximation, and thereby fully captures the physics of charge separation. Note that in this model the ion and electron fluids are coupled exclusively through electromagnetic fields, such that collisional effects are neglected. For the computational results presented here, $M_i/M_e = 25$ unless otherwise noted. The mass ratio is chosen to ensure consistency with kinetic simulations, in which computational cost prohibits the use of larger mass ratios. Because the KH instability is driven by inertia of the heavier fluid, the exact value of the mass ratio is not expected to play a significant role – this is verified to be the case in simulation results presented in Sec. IV A.

To study the linear and nonlinear behavior of KH instabilities in nonuniform magnetized plasmas, the governing equation system of the two-fluid plasma model is solved using a discontinuous Galerkin finite element method[46–48] within the WARPXM (Washington Approximate Riemann Plasma) code framework. The simulations use third-order polynomials for the spatial representation within each triangular element and a third-order strong stability-preserving Runge-Kutta method[49] for the temporal advance.

2. Initial conditions, boundary conditions, and parameters

Simulations are initialized with a shear layer equilibrium, with velocity shear in $x \in [-d, d]$. The equilibrium number density profiles, magnetic field, x-directed electric field, and y-directed flow velocity profiles vary only along the x coordinate. In equilibrium, y-directed electric field and the x-directed flow are both zero, and ions and electrons have equal and uniform temperatures with $T = T_e = T_i$. The equilibrium ion number density profile is chosen to be a smooth analog of the density profile considered in the linear theory analysis – given by Eq. (16), such that

$$n_i(x)\big|_{t=0} = \left(1 + \exp\left(\frac{2x}{d}\right)\right)^{\frac{bd}{2}} \tag{29}$$

and hence

$$\frac{1}{n_i}\frac{\partial n_i}{\partial x} = \frac{b}{2}\left(1 + \tanh\left(\frac{x}{d}\right)\right). \tag{30}$$

Like the density profile in the Hall-MHD analysis – see Eq. (16), the density profile given in Eq. (29) has the property that $\nabla n_i/n_i \approx 0$ for $x \leq -d$ and $\nabla n_i/n_i \approx b$ for $x \geq d$. Unlike the density profile of Eq. (16), however, the density profile of Eq. (29) varies inside the shear layer – see Fig. 5. Thus there is diamagnetic drift inside the shear layer. The equilibrium electric field is chosen to have the form

$$E_x(x)\big|_{t=0} = \frac{E_0}{2}\left(1 + \tanh\left(\frac{x}{d}\right)\right) + c_E, \tag{31}$$

where E_0 and c_E are constants. The value of c_E depends on the desired frame of reference, which can be informed by the plasma application of interest. For a uniform density profile where $b = 0$, the constant c_E is chosen to have a value of $-E_0/2$, which results in an odd-symmetry $E \times B$ velocity profile and hence an average flow velocity of zero. For nonuniform ion density profiles where $b \neq 0$, c_E is set to zero, which results in a non-zero average $E \times B$ flow velocity, as is characteristic of near-electrode plasmas in MITLs – see Fig. 1.

The equilibrium electron number density n_e is obtained by substituting Eq. (29) and Eq. (31) into Gauss's law in Eq. (27). Summing the electron and ion force balance equations, substituting in Gauss's law and steady-state Ampere's law (Eq. (25)), and integrating over the interval $[x_0, x]$ yields an expression for the equilibrium magnetic field,

$$B_z(x)\big|_{t=0} = \frac{B_z(x_0)}{|B_z(x_0)|}\left(-2T\Big[n_e + n_i\Big]_{x_0}^{x} + \Big[E_x^2\Big]_{x_0}^{x} + [B_z(x_0)]^2\right)^{1/2}. \tag{32}$$

The factor $B_z(x_0)/|B_z(x_0)|$ accounts for the direction of the magnetic field. For convenience we choose $x_0 = 0$ and, consistent with the nondimensionalization, we set $B_z(x_0) = 1$ for near-anode plasmas and $B_z(x_0) = -1$ for near-cathode plasmas. Equilibrium y-directed drift velocities for ions and electrons are obtained from one-dimensional force balance for each species. The profiles given in Eq. (29), Eq. (31), and Eq. (32) and the choice of constants T, E_0, b, and d along with magnetization, which is set by Ω_p/ω_{pp}, fully determine the initial equilibrium state.

The electromagnetic two-fluid plasma equilibrium is perturbed by introducing a transverse velocity,

$$u_{sx}(x, y)\big|_{t=0} = 10^{-6}\exp\left(-\frac{x^6}{d^6}\right)\cos\left(k_y y\right). \tag{33}$$

The exponential term in Eq. (33) ensures that the perturbation is localized around the shear layer so as to isolate the physics of interest and avoid exciting additional dynamics. The perturbation wavenumber k_y is chosen to satisfy $k_y d = 0.4$, which, according to the analysis in Sec. II, is close to the fastest growing mode for the density profiles of interest. The simulation domain is defined in nondimensional units, such that $x, y \in [-L_x/2, L_x/2] \times$

$[-L_y/2, L_y/2]$, with $L_x = 1$ and $L_y = 2\pi/k_y$. The simulation domain is periodic in the y direction and has impermeable conducting wall boundaries at $x = \pm L_x/2$, where $u_{sx} = E_y = E_z = B_x = 0$. Dirichlet boundary conditions are set for E_x, B_y, and B_z at $x = \pm L_x/2$, such that these field components retain initial condition values at these boundaries for all time. The rectangular domain is discretized into 256×256 elements.

For our computational study, we perform two-fluid simulations for five parameter cases given in Table I, denoted by *A0*, *A1*, *A2*, *A3*, and *A4*. Case *A0* is a uniform ion density configuration with $bd = 0$, while the other cases involve nonuniform density profiles with $bd = \{-0.5, -1.0\}$ at different levels of magnetization $\Omega_p/\omega_{pp} = \{1.0, 2.0\}$. Nondimensional simulation parameters are chosen to be consistent with the broad range of characteristic experimental parameters described in Sec. I. All cases in Table I correspond to near-anode plasmas, shown schematically in Fig. 1(a), where the ion diamagnetic drift is in the same direction as the $E \times B$ drift and vorticity is antiparallel to the magnetic field. Near-cathode plasmas are discussed in Sec. IV A. In all cases, the wall boundaries are situated sufficiently far away from the shear layer, such that they have a negligible effect on the evolution of the single-mode KH instability – as indicated by the linear theory analysis in Sec. II and verified by performing two-fluid simulations on a larger domain. Electric field magnitude, set by E_0, is chosen to ensure sufficient shear velocity to observe instability over the time scales we can simulate while also facilitating moderate charge separation and the study thereof. Case *A0* involves the smallest value of E_0 and is thereby the most quasineutral configuration. Equilibrium number density and velocity profiles used to initialize two-fluid simulations for parameter cases *A1* – *A4* are shown in Fig. 5. The magnetic field, which is not shown, is nearly uniform such that its variation across the domain is less than 0.15% for all parameter cases. Plasma $\beta = 2(n_i + n_e)T/B_z^2$ is the ratio of nondimensional thermal pressure to nondimensional magnetic pressure and is evaluated in the high density region. For all parameter cases $\beta \leq 2.5 \times 10^{-3}$.

TABLE I: Parameters for five different cases, denoted by *A0*, *A1*, *A2*, *A3*, and *A4*, which are used to initialize simulations. The cases cover uniform density (*A0*), small (*A1*,*A2*) and large (*A3*,*A4*) density gradients, low (*A0*,*A1*,*A3*) and high (*A2*,*A4*) magnetization. Derived quantities in the lower portion of the table include: the ion Larmor radius r_{Li}; Debye length λ_D; the shear $\omega_s = |\Delta u_{iy}|/(2d)$; the jump Δu_{iy} in the ion drift velocity across the shear layer; the jump in $E \times B$ velocity $\Delta u_{E\times B}$ across the shear layer; plasma β, which is the ratio of thermal pressure to magnetic pressure; and the effective shear layer half-width d_{eff} in kinetic simulations.

Parameter	**Simulation Cases**				
	A0	*A1*	*A2*	*A3*	*A4*
L_x	1.0	1.0	1.0	1.0	1.0
L_y	0.449	0.785	0.785	0.785	0.785
d	1/35	1/20	1/20	1/20	1/20
b	0.0	-10.0	-10.0	-20.0	-20.0
T	1.63e-4	6.25e-4	6.25e-4	6.25e-4	6.25e-4
E_0	5.60e-3	2.00e-2	2.00e-2	2.00e-2	2.00e-2
Ω_p/ω_{pp}	1.00	1.00	2.00	1.00	2.00
$B_z\|_{x=0}$	1.00	1.00	1.00	1.00	1.00
$k_y d$	0.4	0.4	0.4	0.4	0.4
bd	0	-0.50	-0.50	-1.00	-1.00
r_{Li}/d	0.448	0.500	0.250	0.500	0.250
λ_D/d	0.45	0.50	0.50	0.50	0.50
ω_s/ω_{pp}	0.1960	0.2625	0.1312	0.3250	0.1625
Ω_p/ω_s	5.10	3.81	15.24	3.08	12.31
Δu_{iy}	-0.0112	-0.0263	-0.0131	-0.0325	-0.0163
$(\Delta u_{E\times B})/(\Delta u_{iy})$	1.000	0.760	0.762	0.615	0.615
$\beta\|_{x=-L_x/2}$	6.52e-4	2.50e-3	2.50e-3	2.50e-3	2.50e-3
d_{eff} (kinetic only)	-	0.068	0.055	0.070	0.055

B. Electrostatic kinetic simulations

1. Governing equations and solver

Kinetic simulations provide a further generalization of the treatments described in Secs. II and III A. By representing each species as a distribution function $f_s(\boldsymbol{x}, \boldsymbol{v}, t)$ in phase space, a kinetic treatment fully captures finite Larmor radius (FLR) effects, including pressure anisotropies and non-Maxwellian distribution functions. For the low-beta collisionless two-species plasmas under consideration, the evolution of each distribution function is described by the nondimensionalized Vlasov equation

$$\frac{\partial f_s}{\partial t} + \boldsymbol{v} \cdot \frac{\partial f_s}{\partial \boldsymbol{x}} + \frac{Z_s}{M_s} \left(\boldsymbol{E} + \frac{\Omega_p}{\omega_{pp}} \boldsymbol{v} \times \hat{\boldsymbol{z}} \right) \cdot \frac{\partial f_s}{\partial \boldsymbol{v}} = 0 \tag{34}$$

and the nondimensionalized Poisson equation,

$$-\nabla^2 \phi = \sum_s Z_s n_s \tag{35}$$

where $\hat{\boldsymbol{z}}$ is the unit vector along the uniform and fixed magnetic field, ϕ is the electrostatic potential, and $\boldsymbol{E} = -\nabla\phi$ is the electric field. The Vlasov-Poisson system given by Eqs. (34) and (35) uses the same nondimensionalization as the multi-fluid model in Eqs. (21) to (28). The electrostatic potential is in effect normalized to $m_p \omega_{pp}^2 L_0^2 / e$. The species number density n_s is obtained from the zeroth velocity moment of the associated distribution function,

$$n_s = \int f_s d\boldsymbol{v}. \tag{36}$$

For x-directed motion, the species momentum $M_s n_s u_{sx}$, kinetic energy W_{sx}, and thermal energy U_{sx} are obtained from the first and second velocity moments, such that

$$M_s n_s u_{sx} = M_s \int v_x f_s d\boldsymbol{v}, \tag{37}$$

$$W_{sx} = \frac{1}{2} M_s n_s u_{sx}^2, \tag{38}$$

$$U_{sx} = \frac{1}{2} M_s \int v_x^2 f_s d\boldsymbol{v} - W_{sx}. \tag{39}$$

Analogously, the momentum and kinetic energy terms associated with y-directed motion can also be evaluated. Species temperature associated with x-directed motion is $T_{sx} = U_{sx}/n_s$, and the total species temperature for a two-dimensional plasma is $T_s = T_{sx} + T_{sy}$.

As in two-fluid simulation, the level of magnetization is set by the ratio Ω_p/ω_{pp}. The assumption of electrostatic and magnetostatic fields implies that magnetic fields from plasma currents are negligible compared to the background magnetic field. This treatment of fields is distinct from the electromagnetic treatment used in the two-fluid description of Sec. III A. For our computational study, the Vlasov-Poisson equation system given by Eq. (34) and Eq. (35) is solved on a structured grid in (x, y, v_x, v_y) phase space using an unsplit conservative fourth-order finite-volume discretization[50–52]. The discretization uses a fifth-order upwind reconstruction of the primary variable and a fourth-order quadrature rule for computing fluxes. The solver has been applied to magnetized plasmas with significant FLR effects[35,50] and has been benchmarked in Cartesian[50] and cylindrical geometries[52]. The solver is also able to preserve complex equilibria[35], which makes it suitable for the study of isolated KH instability physics.

2. Initial conditions, boundary conditions, and parameters

When Larmor radii and gradient scale lengths are comparable, two-fluid equilibria can be poor approximations to kinetic equilibria[19,30,34,35] and oft-used Maxwellian distribution functions[18,19,28–30], which do not satisfy the steady-state Vlasov-Poisson or Vlasov-Maxwell equation system, can introduce spurious dynamics[19,30,33,34]. For example, in the presence of FLR effects, the use of two-fluid equilibria to initialize electrostatic kinetic simulations leads to: significant departure from the initialized state; the excitation of lower-hybrid and upper-hybrid waves; and the formation of sheaths near boundaries. Approximate kinetic equilibria can also result in generation and propagation of waves in time-dependent simulations[35]. The lack of kinetic equilibria is often identified as an impediment to the detailed study of kinetic physics in KH instabilities[19,30,33,34]. To address this issue and to construct self-consistent two-species kinetic equilibria that satisfy the steady-state governing equations, encapsulate finite Larmor radius effects, and can be customized to have density and electric field profiles that are consistent with the two-fluid equilibria described in Sec. III A, we employ the ordinary differential equation method described in Ref. 35. The method relies on using constants of motion to construct auxiliary distribution functions that are close to equilibrium and numerically solving a nonlinear Poisson equation to obtain exact equilibrium distribution functions. The initialization of exact kinetic equilibria, wherein there are no propagating waves and no boundary dynamics, is advantageous because it facilitates the study of isolated physics in experimentally-relevant conditions, such that the driving mechanism(s) for a targeted phenomenon – here the KH instability – can be readily identified. The kinetic equilibria employed here thereby enable detailed quantitative comparisons with fluid simulations and likewise with linear theory.

Kinetic equilibria are constructed as follows. Let the desired ion density profile $g_i(x)$ be the analytic function given in Eq. (29), such that

$$g_i(x) = \left(1 + \exp\left(\frac{2x}{d}\right)\right)^{\frac{bd}{2}} \tag{40}$$

and let the desired electrostatic potential profile ϕ^* be consistent with the electric field profile given in Eq. (31), such that

$$\phi^*(x) = -\frac{E_0 d}{2} \log\left(1 + \exp\left(\frac{2x}{d}\right)\right). \tag{41}$$

The auxiliary ion and electron distribution functions are constructed from g_i and ϕ^*, such that

$$f_i^{aux} = \left[g_i\left(X\right) \exp\left(\frac{Z_i \phi^*\left(X\right)}{T}\right)\right]_{X=p_i} \times \frac{M_i}{2\pi T} \exp\left(-\frac{M_i(v_x^2 + v_y^2)}{2T} - \frac{Z_i \phi^*(x)}{T}\right) \tag{42}$$

$$f_e^{aux} = \left[\left(Z_i n_i^{aux,fit}(X) + \frac{\partial^2 \phi^*(X)}{\partial X^2}\right) \exp\left(\frac{Z_e \phi^*\left(X\right)}{T}\right)\right]_{X=p_e} \times \frac{M_e}{2\pi T} \exp\left(-\frac{M_e(v_x^2 + v_y^2)}{2T} - \frac{Z_e \phi^*(x)}{T}\right), \tag{43}$$

where $n_i^{aux,fit}$ is an analytic fit to the discretely-computed zeroth velocity moment of f_i^{aux}, $p_s = x + v_y/(\Omega_s/\omega_{pp})$ is the scaled canonical momentum for species s, and the nondimensionalized species cyclotron frequency Ω_s/ω_{pp} can be positive or negative depending on the species charge Z_s. The exact equilibrium distribution functions can be expressed in terms of the auxiliary distribution functions and the equilibrium potential ϕ, which is obtained by numerically solving the nonlinear Poisson equation

$$-\frac{\partial^2 \phi}{\partial x^2} = Z_i n_i^{aux} \exp\left(\frac{Z_i(\phi^* - \phi)}{T}\right) + Z_e n_e^{aux} \exp\left(\frac{Z_e(\phi^* - \phi)}{T}\right), \tag{44}$$

where n_s^{aux} is the numerically-computed zeroth velocity moment of f_s^{aux}. The Newton method, with $\phi = \phi^*$ as the initial guess, is used to solve for ϕ and Dirichlet boundary conditions are assumed for the equilibrium potential, such that $\phi(\pm L_x/2) = \phi^*(\pm L_x/2)$.

Thus the equilibrium distribution function for each species is given by

$$f_s = f_s^{aux} \exp\left(\frac{Z_s(\phi^* - \phi)}{T}\right). \tag{45}$$

Reference 35 presents further details regarding equilibrium construction for density and potential profiles given by Eq. (40) and Eq. (41), respectively. For the parameter cases considered here, the relative difference between ϕ and ϕ^* is less than 1%. Notably even small differences between ϕ and ϕ^* can strongly affect ion number density profiles, which is why solving for the equilibrium potential is important[35].

Unlike two-fluid simulations, where the x-directed velocity of both species is perturbed, the kinetic equilibrium is perturbed by multiplying the equilibrium electron distribution function f_e by a factor $(1+\epsilon)$, where

$$\epsilon = 2.0 \times 10^{-4} \sin\left(\frac{2\pi y}{L_y}\right) \exp\left(-\frac{x^6}{d^6}\right). \tag{46}$$

As in two-fluid simulations, the perturbation is localized around the shear layer so as to avoid introducing waves and sheaths near the boundaries. The perturbation wavenumber k_y is chosen to satisfy $k_y d = 0.4$ to excite the fastest growing mode. The phase space simulation domain is $[-L_x/2, L_x/2] \times [-L_y/2, L_y/2] \times [-v_{\max,s}, v_{\max,s}] \times [-v_{\max,s}, v_{\max,s}]$, where $L_x = 1, L_y = 2\pi/k_y, v_{\max,e} = 1.0, v_{\max,i} = 0.2$. The domain is periodic in the $\hat{y}$ direction and reflecting wall boundary conditions are applied at $x = \pm L_x/2$ – see Ref. 51 for details. Dirichlet boundary conditions are used for the potential, such that $\phi(\pm L_x/2) = \phi^*(\pm L_x/2)$ for all time. The velocity domain is set to have zero-flux boundary conditions, which has no effect on the physics of the simulation provided that the value of the distribution function is sufficiently close to zero at these boundaries[50,52], as is the case here. A resolution of $N_x \times N_y \times N_{v_x} \times N_{v_y} = 256 \times 64 \times 96 \times 96$ cells is used in all cases.

For our computational study, we perform four kinetic simulations corresponding to the *A1*, *A2*, *A3*, and *A4* parameter cases given in Table I. Much like the two-fluid initialization, the choice of constants T, E_0, b, d and magnetization Ω_p/ω_{pp}, determine the initial equilibrium state. Finite Larmor motion, which is encapsulated in the construction of the kinetic equilibrium initial condition, results in a shear layer that is not identical to the two-fluid model shear layer. See Fig. 5 for a comparison of kinetic and two-fluid equilibrium profiles. One difference is that the kinetic shear layer is more diffuse and its effective half-width d_{eff}, which is listed in Table I, does not match the half-width of the two-fluid shear layer. Likewise, kinetic equilibria exhibit an expected temperature anisotropy[34,35] that is not present

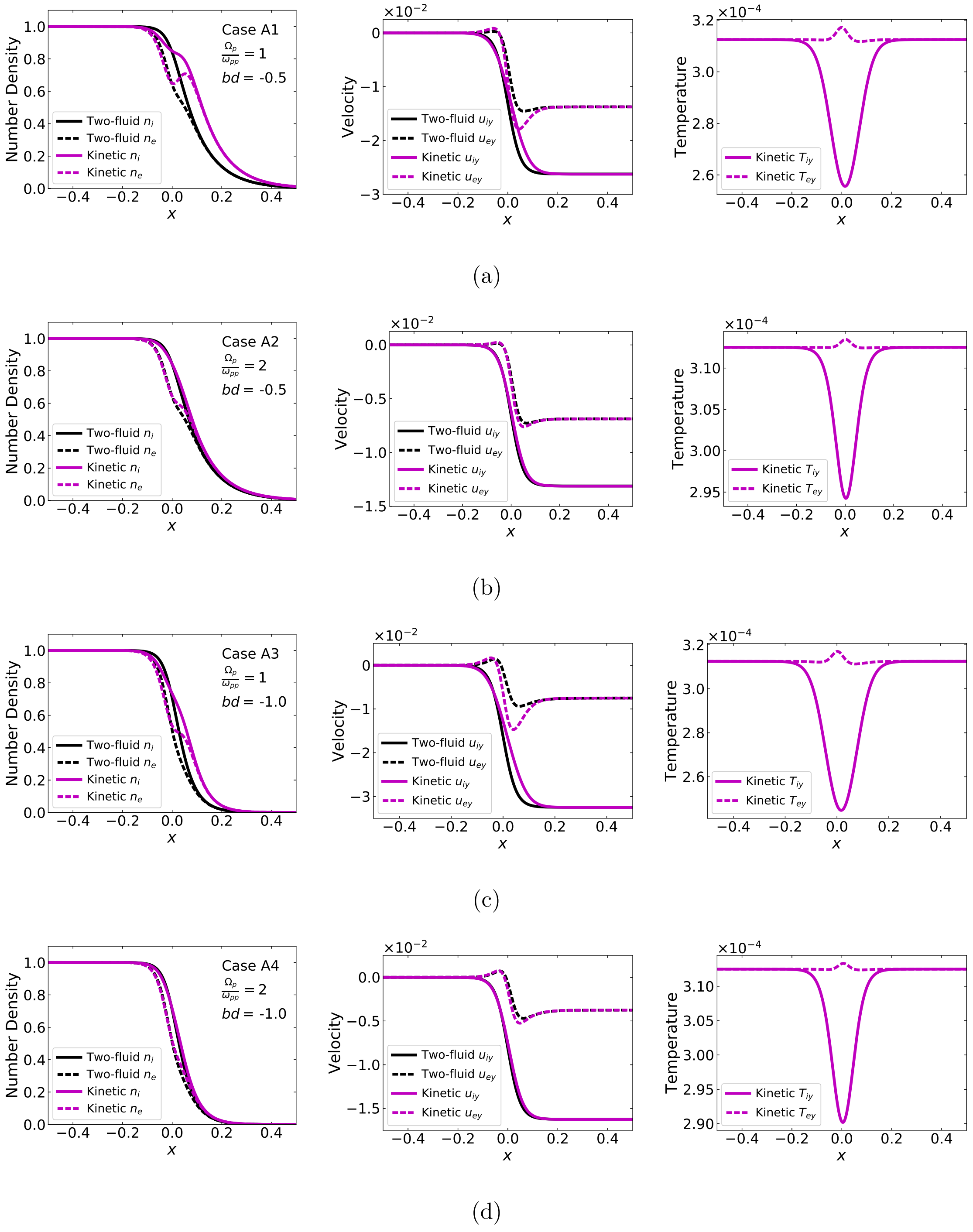

(a)

(b)

(c)

(d)

FIG. 5: Equilibrium shear layer profiles for ions (solid lines) and electrons (dashed lines) used as initial conditions for two-fluid simulations (black) and kinetic simulations (magenta) for parameter cases (a) *A1*, (b) *A2*, (c) *A3*, and (d) *A4*, which are outlined in Table I. Shown are number density and drift velocity profiles for two-fluid and kinetic equilibrium initializations. Also shown are plots of temperature T_{sy} for kinetic simulations. In two-fluid simulations initial temperature (not shown) is uniform and isotropic such that $T = 2T_{sx} = 2T_{sy} = 6.25 \times 10^{-4}$, whereas in kinetic simulations $T_{sx} = 3.125 \times 10^{-4}$ is uniform, but temperature is anisotropic such that $T_{sx} \neq T_{sy}$ in the shear layer. FLR effects encapsulated in the kinetic equilibria cause the density and velocity profiles to be more diffuse when compared to the two-fluid representation. As magnetization is increased from $\Omega_p/\omega_{pp} = 1.0$ to $\Omega_p/\omega_{pp} = 2.0$, the kinetic equilibrium converges to the two-fluid equilibrium.

in two-fluid equilibria, such that the temperature T_{sx} associated with x-directed thermal motion is uniform with a value of 3.125×10^{-4}, whereas the temperature T_{sy} associated with y-directed thermal motion varies in the shear layer. Nevertheless, the kinetic and two-fluid equilibria are consistent to within about one ion Larmor orbit. This means that as magnetization increases, the role of FLR effects diminish, and the kinetic equilibrium approaches the two-fluid equilibrium[35] – as shown in Fig. 5. Thus for kinetic simulations, the parameters outlined in Table I should be treated as guiding center parameters. Kinetic equilibria whose guiding center profiles match the two-fluid equilibria, as they do here, facilitate the isolated study of KH instability physics in the presence of FLR effects and enable systematic cross-comparisons between the two models.

IV. TWO-FLUID AND KINETIC SIMULATIONS OF THE KELVIN-HELMHOLTZ INSTABILITY

The evolution of the KH instability in simulations can be roughly separated into a linear phase, during which the instability grows exponentially, and a nonlinear phase, during which the large scale dynamics – including the formation of the characteristic vortex feature – are observed. We proceed to examine the linear and nonlinear phases separately and assess growth rates, oscillation frequencies, and transport properties. We rescale simulation units to match the units used in the Hall-MHD analysis in Sec. II. This choice of units allows us to separate shear – on which the KH instability strongly depends – from other variables of interest. Consequently, for the analysis presented in this section, time is measured in units of shear ω_s and distance is measured in units of shear-layer half-width d, which are given in Table I for each parameter case.

A. Linear phase

The linear stage of the instability is characterized by the exponential growth in the amplitude of the x-directed drift velocity for ions and electrons. In simulations this is accompanied by the exponential growth in the amplitude of the y-directed electric field. To determine the instability growth rate and oscillation frequency, the magnitude of the x-directed ion velocity $|u_{ix}|$ is evaluated locally at the center of the domain and is tracked as a function of time. Growth rates from simulations can also be evaluated by tracking the spatial integral of E_y^2 or u_{ix}^2 as a function of time; however, these integrated quantities do not retain oscillation frequency information and consequently are not used here. Temporal evolution of $|u_{ix}|$ for parameter cases *A0*, *A1*, and *A2* is shown in Fig. 6. Note that the *A0* parameter case is simulated using only the two-fluid solver. For all the parameter cases outlined in Table I, growth rates and oscillation frequencies from Hall-MHD theory of Sec. II, two-fluid simulations, and kinetic simulations are presented in Table II.

Growth rates in Table II show that for a uniform ion density configuration with a small amount of charge separation, i.e. parameter case *A0* where $\max(n_i - n_e)/n_i = 0.056$, the two-fluid simulation agrees with the Hall-MHD theoretical prediction. The simulation oscillation frequency is zero, as expected for a configuration in which $u_{iy}(x)|_{t=0}$ has odd symmetry, and the simulation growth rate is 6% smaller than the growth rate predicted by Hall-MHD linear theory – see Fig. 6(a). The small discrepancy in growth rates between the two models can be attributed to charge separation in the two-fluid equilibrium shear layer.

Table II also shows that for parameter cases that have nonuniform ion density profiles and that are not charge-neutral, two-fluid and kinetic simulations do not agree with Hall-MHD theory. For these cases, the growth rates predicted by Hall MHD are significantly larger than the growth rates in two-fluid simulations, which are larger than the growth rates in kinetic simulations. The relative difference between Hall-MHD and two-fluid growth rates are 26%, 43%, 47%, and 72% for parameter cases *A1*, *A2*, *A3*, and *A4*, respectively. The largest discrepancies are associated with cases *A3* and *A4*, which have the largest density gradients. Increasing magnetization results in more discrepancy between Hall-MHD theory predictions and two-fluid simulation results. Interestingly, the trend observed in simulations is that growth rate decreases as density variation at the edge of the shear layer increases (i.e. as bd becomes more negative), which contradicts the trends predicted by Hall-MHD theory. In particular, when changing the density profile from $bd = -0.5$ to a steeper density profile with $bd = -1.0$ (i.e. when going from case *A1* to *A3* or case *A2* to *A4*), Hall MHD predicts about a 2% increase in the growth rate, whereas two-fluid and kinetic simulations show about a 14-21% decrease in growth rate. This discrepancy suggests that in addition to velocity shear and fluid inertia, charge distribution and density variation in the shear layer (which are not accounted for in the Hall-MHD analysis) can also strongly affect KH instability growth rates.

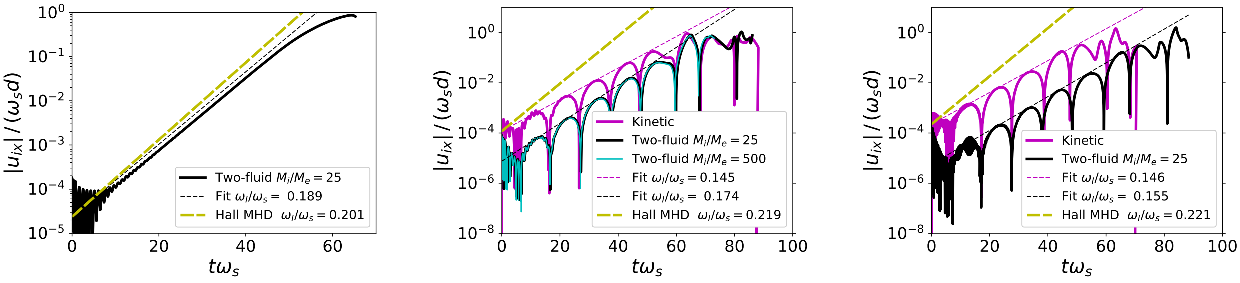

(a) (b) (c)

FIG. 6: Evolution of the x-directed ion velocity $|u_{ix}|$ evaluated in the middle of the simulation domain at $x = 0, y = 0$. (a) For case *A0* with $b = 0$ and $\Omega_p/\omega_{pp} = 1$, ion number density is uniform, the plasma is quasineutral, and the KH instability exhibits pure growth without oscillation. The growth rate obtained from two-fluid simulations is in close agreement with the growth rate predicted by linear Hall-MHD theory. (b) For case *A1* with $bd = -0.5$ and $\Omega_p/\omega_{pp} = 1$, the equilibrium ion number density is nonuniform and magnetization is relatively small, and two-fluid simulations exhibit larger growth rates than the kinetic simulations. Simulation growth rates do not agree with growth rates from Hall-MHD analysis. Two-fluid simulations with mass ratios of $M_i/M_e = 25$ and $M_i/M_e = 500$ produce virtually the same results. (c) For case *A2* with $bd = -0.5$ and $\Omega_p/\omega_{pp} = 2$, the equilibrium ion number density is nonuniform and magnetization is large. Two-fluid and kinetic simulations exhibit similar growth rates, which are smaller than those predicted by Hall-MHD analysis. Oscillation frequencies in two-fluid and kinetic simulations are in close agreement. The different cases are outlined in Table I.

To further gauge the effects of density gradients and charge separation on growth rates, a two-fluid simulation of a modified *A1* configuration was performed, wherein the same parameters and the same equilibrium construction were used, except the polarities of the equilibrium electric and magnetic fields were reversed, such that $E_0 = -0.02$ and $B_z|_{x=0} = -1$. This modified configuration, which we will denoted by *C1*, has the same $E \times B$ drift velocity as case *A1*, but the direction of the diamagnetic drift for each species is reversed. In the context of anode-cathode gaps, case *A1* represents a near-anode plasma and case *C1* represents a near-cathode plasma – see Fig. 1 for a schematic comparing these two configurations. Unlike case *A1*, case *C1* has a negative net charge, an ion diamagnetic drift

TABLE II: Growth rates and oscillation frequencies obtained from Hall-MHD theory, two-fluid simulations, and kinetic simulations for five different parameter cases. See Table I for the complete set of parameters. The oscillation frequencies in simulations are negative since the mode propagates in the $-\hat{y}$ direction. For cases *A1*, *A2*, *A3*, and *A4* oscillation frequency from Hall-MHD theory has been Doppler shifted by $k_y \Delta u_{iy}/2$ to account for the difference in frames of reference.

Frequency	**Model Description**	**Simulation Cases**				
		A0	*A1*	*A2*	*A3*	*A4*
Oscillation frequency ω_R/ω_s	Hall-MHD theory	0	-0.254	-0.256	-0.293	-0.295
	Two-fluid simulation	0	-0.306	-0.305	-0.232	-0.243
	Kinetic simulation	-	-0.294	-0.299	-0.232	-0.239
Growth rate ω_I/ω_s	Hall-MHD theory	0.201	0.219	0.221	0.223	0.225
	Two-fluid simulation	0.189	0.174	0.155	0.152	0.131
	Kinetic simulation	-	0.145	0.146	0.119	0.121

that opposes the $E \times B$ drift, and vorticity that is aligned with the magnetic field. For case *C1* the two-fluid simulation growth rate is $\omega_I/\omega_s = 0.271$, which is 19% higher than that predicted by Hall MHD. If the magnitude of the electric field is halved in case *C1* then the two-fluid growth rate is $\omega_I/\omega_s = 0.502$, which is 56% higher than that predicted by Hall MHD. The fact that growth rate, normalized to shear, is much larger for case *C1* than case *A1* suggests that the orientation and magnitude of the ion diamagnetic drift relative to the $E \times B$ flow can have a strong effect on the evolution of the KH instability. In particular, when ion diamagnetic drift opposes $E \times B$ drift, larger growth rates, per unit shear, are observed. By contrast, when ion diamagnetic drift is aligned with $E \times B$ drift – as in cases *A1*, *A2*, *A3*, and *A4*, smaller growth rates are observed. Near-anode and near-cathode plasmas thus behave differently in the presence of velocity shear.

The observed trend in growth rates is consistent with the findings of FLR MHD[21] and kinetic simulation[29] studies of nonuniform plasmas. This trend is often described in terms of the relative orientation of vorticity $\boldsymbol{w} = \nabla \times \boldsymbol{u}$, i.e. when $\boldsymbol{w} \cdot \boldsymbol{B} > 0$ larger growth rates are observed than for the case where $\boldsymbol{w} \cdot \boldsymbol{B} < 0$. Kinetic simulations of KH instabilities in uniform-density plasmas[19,30] have also indicated a dependence on the sign of $\boldsymbol{w} \cdot \boldsymbol{B}$, however this finding may be partially attributed to density gradients in the shear layer, which are either inherently present in kinetic shear layer equilibria[34,53] or which form due to finite Larmor motion when a kinetic equilibrium is not initialized[19,30]. Notably, in the absence of ion density gradients and FLR effects, the orientation of vorticity is inconsequential. To verify this, a two-fluid simulation of a modified *A0* configuration was performed, wherein the same uniform ion density configuration was modeled, but with polarities of the equilibrium electric and magnetic fields reversed. Unlike case *A0*, the modified configuration, denoted by *C0*, has a small negative net charge and vorticity that is aligned with the magnetic field. The resulting growth rate for case *C0* is identical to the growth rate for case *A0*, indicating that the orientation of vorticity relative to the magnetic field does not play a role for uniform density plasmas. This result suggests that the sign of $\boldsymbol{w} \cdot \boldsymbol{B}$ is not the most relevant indicator of enhanced/diminished growth for KH instabilities, and that charge distribution and density variation are more consequential.

Two-fluid and kinetic simulations indicate that the orientation of diamagnetic drift relative to $E \times B$ drift affects the distribution of charge density during the linear phase of the instability and can modify the spatial structure of the fastest growing mode. In particular, charge redistribution leads to different parts of the shear layer having a larger-amplitude y-directed electric field E_y. Figure 7 shows the net change in charge density $\Delta\rho$ and the y-directed electric field during the linear phase of the KH instability for cases *A1* and *C1*. In case *A1* the redistribution of charge causes E_y to be slightly amplified at the left edge of the shear layer, whereas in case *C1* the redistribution of charge causes E_y to be amplified at the right edge of the shear layer. Since the KH instability is driven by inertia, and since the y-directed electric field is what ultimately leads to the advective motion of the high-density plasma, having an enhanced E_y at the right edge of the shear layer – where there is a "free" boundary – results in a more unstable configuration. From the continuity equation for each species, the accumulation of charge ρ can be quantified in terms of the divergence of the current $\boldsymbol{j} = \sum_s q_s n_s \boldsymbol{u}_s$. Assuming a uniform magnetic field and isotropic pressure, the time derivative of the local charge density is

$$\frac{\partial \rho}{\partial t} = -\nabla \cdot \boldsymbol{j} = -\nabla \cdot \left[\rho \frac{\boldsymbol{E} \times \boldsymbol{B}}{B^2} - \frac{m_i n_i}{B^2} \frac{\partial \boldsymbol{u}_i}{\partial t} \times \boldsymbol{B} \right], \tag{47}$$

where the first term in the square brackets is the contribution from $E \times B$ drift and the second term is the contribution from polarization drift, which is associated with the inertia of the particles. Since $m_e \ll m_i$, we have dropped the electron contribution to the polarization drift. Note that in the case of isotropic pressure, diamagnetic drift does not contribute to charge accumulations since the associated current is always divergence free. Equation (47) can be reexpressed as

$$\frac{\partial \rho}{\partial t} = -\nabla \cdot \left[\rho \frac{\boldsymbol{E} \times \boldsymbol{B}}{B^2}\right] + \frac{m_i}{B^2}\left[n_i \boldsymbol{B} \cdot \left(\nabla \times \frac{\partial \boldsymbol{u}_i}{\partial t}\right) - (\nabla n_i \times \boldsymbol{B}) \cdot \frac{\partial \boldsymbol{u}_i}{\partial t}\right]. \tag{48}$$

Equation (48) shows that charge density in the presence of $E \times B$ drift and ion density gradients can contribute to local charge accumulation, and hence to the local amplification of E_y. Two-fluid simulations indicate that changing the polarity of the electric and magnetic fields has a noticeable effect only for the case of nonuniform ion density, which indicates that it is the last term in Eq. (48) that results in asymmetry of E_y shown in Fig. 7. Equation (48) also confirms the finding that the orientation of $\nabla n_i \times \boldsymbol{B}$, which is correlated with diamagnetic drift, is consequential. Notably the $\nabla n_i \times \boldsymbol{B}$ term will lead to charge accumulation even in the absence of diamagnetic drift, e.g. even when temperature is zero.

Kinetic simulations, which in addition to capturing two-fluid physics also capture FLR effects, exhibit smaller growth rates than two-fluid simulations. The relative difference between two-fluid and kinetic growth rates are 20%, 6%, 28%, and 8% for parameter cases *A1*, *A2*, *A3*, and *A4*, respectively. Two-fluid and kinetic simulation results have better agreement for cases with higher magnetization – *A2* and *A4*, where the ion Larmor radius is a small fraction of the shear layer half-width, i.e. $r_{Li}/d = 0.25$. For cases *A1* and *A3*, where $r_{Li}/d = 0.5$, FLR effects are more significant and lead to larger disagreement between two-fluid and kinetic simulations. The stabilization of KH instabilities due to FLR effects, particularly as r_{Li}/d increases, is consistent with previous studies[19,21,30].

It is found that the difference in the treatment of electromagnetic fields in two-fluid simulations, as compared to kinetic simulations, does not play a significant role. In two-fluid simulations, which encapsulate electromagnetic physics, the magnetic field components (B_x, B_y) are self-consistently evolved and retain a value of zero for all time. The B_z component of the magnetic field changes by less than 0.3% from the initialized profile – even well into the nonlinear stage of the instability. This suggests that the electrostatic and magnetostatic treatment of fields in kinetic simulations is justified for the low-beta ($\beta \leq 2.5 \times 10^{-3}$)

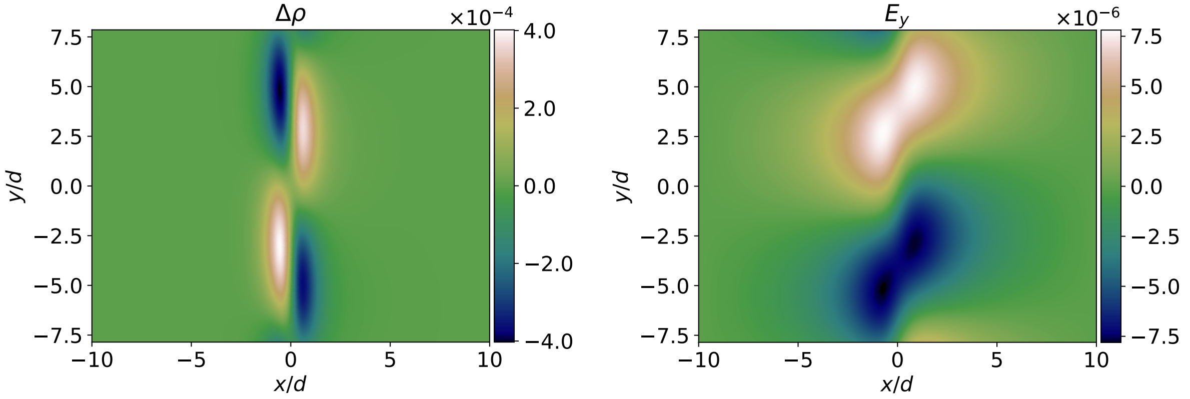

(a) Case *A1* with $B_z|_{x=0} = 1, E_0 = 0.02$

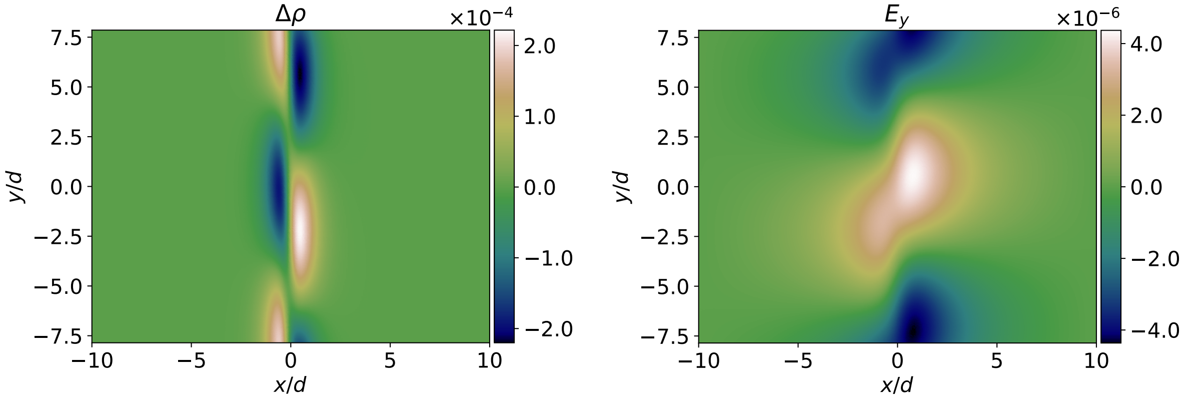

(b) Case *C1* with $B_z|_{x=0} = -1, E_0 = -0.02$

FIG. 7: The net change in the charge density relative to initial time (left) and the E_y component of the electric field (right) from two-fluid simulations of of (a) parameter case *A1* with $B_z|_{x=0} = 1$, $E_0 = 0.02$ and (b) parameter case *C1* with $B_z|_{x=0} = -1$, $E_0 = -0.02$. In case *A1* ion diamagnetic drift is aligned with $E \times B$ drift and the initial configuration has a net positive charge and in case *C1* ion diamagnetic drift opposes $E \times B$ drift and the initial configuration has a net negative charge – see Fig. 1 for a schematic. During the linear phase of the instability, the charge density is redistributed, resulting in localized amplification of E_y. For case *A1* E_y is amplified near the left edge of the shear layer, and for case *C1* E_y is amplified near the right edge of the shear layer.

Amplification of the electric field near the right edge of the shear layer, where ion density transitions from high to low and where the shear layer is more susceptible to attenuation, leads to a more unstable configuration and an enhanced growth rate. In two-fluid simulations the growth rate for case *A1* is $\omega_I/\omega_s = 0.174$ and growth rate for case *C1* is $\omega_I/\omega_s = 0.271$. Thus the redistribution of charge can strongly affect the development of the KH instability.

configurations considered. While the present computational investigation is restricted to the case of $\boldsymbol{k} \cdot \boldsymbol{B} = 0$, electromagnetic effects can become non-negligible if the perturbation wavenumber along the magnetic field is non-zero.[37,54] A non-zero electric field (or current) parallel to the magnetic field can also introduce electromagnetic physics.[37,55,56]

In addition to growth rates, other features of the linear evolution of the KH instability are consistent between the kinetic and two-fluid simulations. As shown in Table II, the oscillation frequency for kinetic simulations is within two percent of the oscillation frequency obtained from two-fluid simulations for parameter cases *A1*, *A2*, *A3*, and *A4*. Oscillation frequencies predicted by Hall-MHD theory agree with two-fluid simulations for the *A0* parameter case, but otherwise have significantly different values. This discrepancy is expected given that two-fluid and kinetic descriptions encapsulate more physics and more waves than Hall MHD. In simulations the nondimensional oscillation frequency is $\omega_R/\omega_s = \pi/(\Delta t_{\min})$, where $\Delta t_{\min}$ is the average time between local minima in the linear evolution of $|u_{ix}|$ versus time. See Fig. 6(a) for case with zero oscillation frequency and Figs. 6(b) and 6(c) for cases with finite oscillation frequencies. The linear stage of the KH instability evolution ends when the instability stops growing exponentially, which occurs when $|u_x|/(\omega_s d)$ reaches a value of ≈ 0.1. As shown in Fig. 6, the time at which this happens in simulations depends on the perturbation and on the details of how the most unstable mode evolves. Notably the form and magnitude of the perturbation is different in two-fluid simulations as compared to kinetic simulations, the unstable eigenmode tends to develop faster in kinetic simulations than in two-fluid simulations, and the growth rate tends to be larger in two-fluid simulations. The eigenmode structures in kinetic and two-fluid simulations are in close agreement and the spatial structure of $E_y(x, y)$, which is shown in Fig. 7, follows closely the spatial structure of $u_x(x, y)$. For nonuniform-density anode configurations shown schematically in Fig. 1(a), the eigenmode structure in simulations (see Fig. 7(a)) closely resembles the Hall-MHD-derived eigenmode structure for a uniform-density plasma (see Fig. 4(a)), except amplitudes tend to be slightly larger on the high-density side of the shear layer. In nonuniform-density cathode configurations (see Fig. 1(b)), the eigenmode structure in simulations (see Fig. 7(b)) resembles the Hall-MHD-derived eigenmode structure for a nonuniform-density plasma (see Fig. 4(b)), with significantly larger amplitudes and wider extent on the low-density side of the shear layer.

On account of computational cost considerations for kinetic simulations and in the interest of consistency, a mass ratio of $M_i/M_e = 25$ was used for all simulation parameter cases outlined in Table I and results presented in Table II. To evaluate the effect of different mass ratios, a two-fluid simulation of the *A1* parameter case was also performed for $M_i/M_e = 500$. The evolution of $|u_{ix}|$ is shown in Fig. 6(b) and the associated growth rate and real frequency is found to be virtually the same as the $M_i/M_e = 25$ mass ratio simulation. Figure 6(b) also shows that $M_i/M_e = 25$ and $M_i/M_e = 500$ simulations result in the same dynamics well into the nonlinear phase of the instability, which suggests that electron inertia does not affect the evolution of the KH instability and using $M_e = 1/25$ is sufficient for practical purposes. This finding is consistent with previous studies that considered mass ratio effects in kinetic simulations of KH instabilities[18,30]. In principle, mass ratio can affect the development of secondary instabilities, which can form during the nonlinear stage and which are not explored here. The end time for simulations is chosen to be before secondary instabilities develop.

While kinetic simulations had two velocity coordinates and hence two degrees of freedom, two-fluid simulations used an adiabatic index of $\gamma = 5/3$, which corresponds to three degrees of freedom. Two-fluid simulations with $\gamma = 2$ and with $\gamma = 5/3$ were compared and the resulting KH instability growth rates were found to be indistinguishable, which is consistent with the findings of previous MHD simulation studies[16].

B. Nonlinear phase and mass transport

In addition to modifying growth rates and oscillation frequencies, two-fluid and kinetic physics also affects the nonlinear phase of the KH instability. The characteristic eddy feature is modified on account of FLR physics, diamagnetic drift, and charge separation, which affect the velocity flow field. The ion number density and the velocity field for ions and electrons from kinetic simulations are shown in Fig. 8 for low- and high-magnetization configurations with large density gradients, i.e. cases *A3* and *A4*. While the eddy structure is similar, density features at low magnetization are more diffuse on account of more significant FLR effects. Ion and electron velocities are aligned in regions where the pressure gradient is low and diamagnetic drift is negligible, e.g. in regions near wall boundaries and in the middle of the eddy. The combined effect of $E \times B$ and polarization drift leads to localized accumulation of charge. For these parameter cases, the initial charge density is positive, and during the onset of the nonlinear phase more positive charge accumulates in the vortex as the

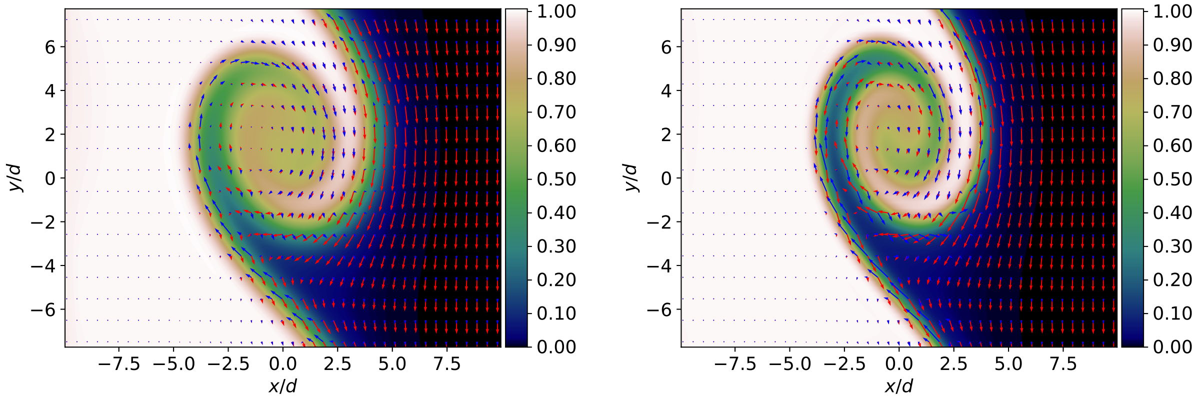

(a) *A3* case with $\frac{\Omega_p}{\omega_{pp}} = 1$, $t\omega_s = 85.8$

(b) *A4* case with $\frac{\Omega_p}{\omega_{pp}} = 2$, $t\omega_s = 83.1$

FIG. 8: Ion number density from kinetic simulations of (a) parameter case *A3* with $\Omega_p/\omega_{pp} = 1$ at time $t\omega_s = 85.8$ and (b) parameter case *A4* with $\Omega_p/\omega_{pp} = 2$ at time $t\omega_s = 83.1$. Parameter cases *A3* and *A4* are outlined in Table I. Ion number density is overplotted with arrows indicating direction and magnitude of ion velocity in red and electron velocity in blue. As the instability evolves the density profile steepens at the leading edge of the eddy. For each species, the largest velocities are in regions where diamagnetic drift and $E \times B$ drift are aligned. Diamagnetic drift dominates the flow field wherever ion and electron velocities have similar magnitudes and opposite directions. FLR effects in the lower magnetization case (*A3*) preclude the formation of fine-scale density features.

instability evolves. In modified configurations, where polarity of the electric and magnetic field are reversed – see Fig. 1 and discussion in Sec. IV A, the initial charge concentration is negative and negative charge accumulates in the vortex. The accumulation of charge is accompanied by the development of a divergent electric field in the middle of the eddy, which leads to enhanced circulatory polarization drift during the initial stage of eddy formation.

The main distinction between two-fluid and kinetic simulations of the KH instability is the presence of FLR effects in the latter. As a result and as noted in previous studies[29,30], kinetic simulations have a lower bound on the gradient scale lengths that can develop during the nonlinear evolution of the KH instability, whereas two-fluid simulations – in the absence of collisional transport terms – do not. Since there is no viscosity in the two-fluid description

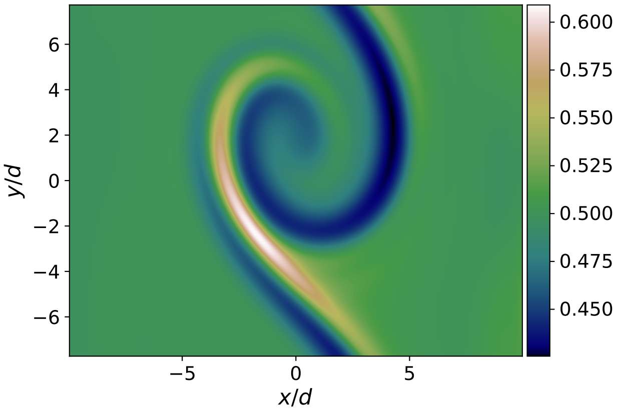

FIG. 9: Nondimensionalized ion Larmor radius r_{Li}/d from kinetic simulations of the *A3* parameter case (see Table I and Fig. 5), plotted as a function of position at time $t\omega_s = 85.8$. Since kinetic simulations are magnetostatic, variation of ion Larmor radius coincides with variation of ion thermal speed. The range of Larmor radii $r_{Li}/d \in [0.426, 0.607]$ is more than a six-fold increase over the range of Larmor radii at initial time, which indicates that the magnetic moment is not conserved and the instability evolution is not adiabatic.

used here, the model does not have a physical dissipation scale, and in principle – though not in numerical simulations – can produce features with infinitesimally small gradient scales. The smallest allowable scale length can affect the local diamagnetic drift and can also have important consequences for secondary KH and Rayleigh-Taylor instabilities, which are not explored here. The propensity of the KH instability to lead to steeper and steeper density variations in two-fluid simulations can also have important consequences for numerics, since the choice of numerical dissipation used to deal with discontinuities can affect the physics that is captured.

In kinetic simulations, the minimum scale length for each species is set by the local Larmor radius. For case *A3* at initial time $r_{Li}/d \in [0.472, 0.500]$, whereas at time $t\omega_s = 85.8$ the range of Larmor radii increases to $r_{Li}/d \in [0.426, 0.607]$. The spatial variation of Larmor radius at time $t\omega_s = 85.8$ is shown in Fig. 9. The largest Larmor orbits are in regions where the low-density plasma infiltrates the high-density region, which is also where sharp density features tend to get smeared out – see Fig. 8. For case *A4* at initial time $r_{Li}/d \in [0.245, 0.250]$, whereas at time $t\omega = 83.1$ the range of Larmor radii increases to $r_{Li}/d \in [0.225, 0.280]$. Note that the initial variation of gyroradii is associated with the anisotropic temperature in the equilibrium shear layer – see Fig. 5. In kinetic simulations, where the magnetic field is uniform and fixed in time, the Larmor radius is proportional to the thermal speed. The magnetic moment, which scales as r_{Ls}^2, is not conserved, which implies that the nonlinear stage of the KH instability is not adiabatic. The nonadiabatic nature of the instability is confirmed in two-fluid simulations, where the initially-uniform ion temperature evolves to have about ±30% variation throughout the domain, while magnetic field variation remains less than 0.3% percent for all time. Locations of global extrema for ion temperatures in two-fluid simulations coincide with the global extrema for ion gyroradii shown in Fig. 9.

An important feature of the KH instability in low-beta configurations is the associated transport of plasma perpendicular to the magnetic field. Mass transport driven by the KH instability is a nonlinear effect and is only present when density is nonuniform across the shear layer. Uniform density profiles or density profiles that have an even symmetry across the shear layer do not result in net mass transport. Figure 10 shows the y-averaged species number density $\langle n_s \rangle_y$ in the nonlinear phase obtained from two-fluid and kinetic simulations for parameter cases *A1* and *A2*, which are outlined in Table I. The y-averaged number density flattens in the middle of the domain as plasma is transported across the shear layer from left to right. This flattening process is observed for all parameter cases. The general features of the y-averaged number densities, including charge separation and spatial extent of the flattening in the $\hat{x}$ direction, are similar for all parameter cases – independent of the model used. The y-averaged number densities in two-fluid and kinetic simulations exhibit better agreement for higher magnetization configurations like case *A2*.

Mass transport can be explicitly quantified from the x-directed momentum, which is one of the primary variables in two-fluid simulations and which can be evaluated from the first velocity moment (see Eq. (37)) of the distribution function(s) in kinetic simulations. The x-directed ion mass flux per unit length in y is simply the y-averaged x-directed ion momentum $\langle M_i n_i u_{ix} \rangle_y$, which is defined as

$$\langle M_i n_i u_{ix} \rangle_y = \frac{M_i}{L_y} \int_{-L_y/2}^{L_y/2} n_i u_{ix} dy, \tag{49}$$

where $M_i = 1$. The mass flux, with u_{ix} normalized to $\omega_s d$, from two-fluid and kinetic simulations is plotted in Fig. 11 as a function of position and time for nonuniform-density parameter cases *A1* and *A2*. As expected, mass flux is only apparent in the nonlinear stage

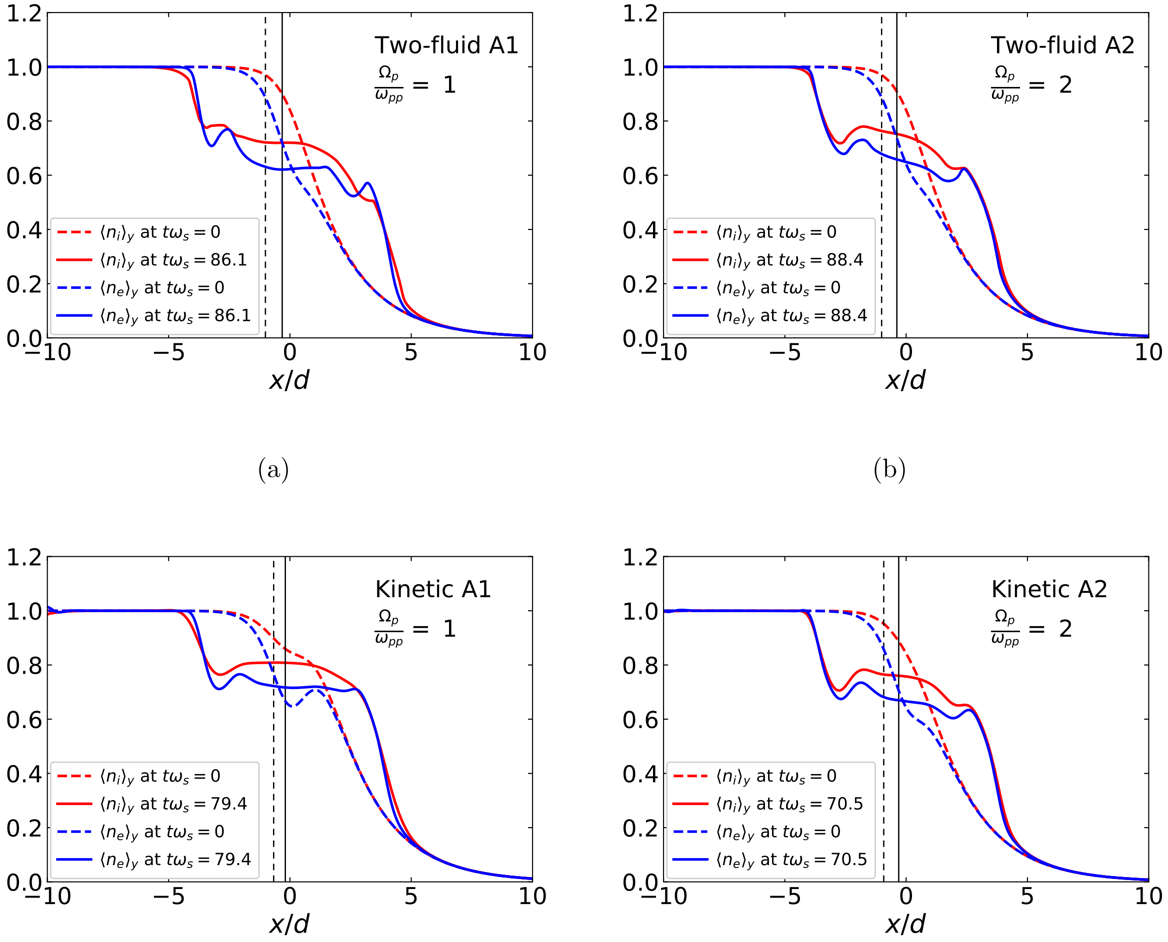

(a)

(b)

(c)

(d)

FIG. 10: The y-averaged species number density $\langle n_s \rangle_y$ plotted at initial and final time for (a) two-fluid simulation of case *A1*, (b) two-fluid simulation of case *A2* , (c) kinetic simulation of case *A1*, and (d) kinetic simulation of case *A2*. Parameter cases *A1* and *A2* are outlined in Table I. The centroid of the ion number density computed over $x/d \in [-4, 4]$, which is the approximate region spanned by the instability, is shown at initial time (black dashed line) and final time (black solid line). During the nonlinear phase of the KH instability, plasma is transported across the shear layer, as indicated by the flattening of the y-averaged number density profiles and the shift in centroid. While the general trends are independent of magnetization and model, plasma transport and the y-averaged number densities from kinetic and two-fluid simulations are in better agreement at higher magnetization. At lower magnetization, the two-fluid simulations exhibit much larger net shift of the plasma, which is due to the shear layer and the density drop-off being slightly offset in the kinetic equilibrium.

of the instability, when $|u_{ix}|/(\omega_s d) \gtrsim 0.1$. Mass flux first occurs in the region where the magnitude of the equilibrium density gradient is largest, which is generally close to the middle of the shear layer. In all simulations, the plasma region with positive mass flux expands approximately linearly in time until it reaches a spatial extent of about four shear layer widths. The factor of four difference between the initial shear layer width and final vortex width is consistent with previous findings[24]. Mass flux tends to reach a maximum value near the right edge of the shear layer. The mass flux ultimately decreases as the instability evolves, but the time-integrated mass flux remains positive for all cases for the time scales simulated, indicating net transport of plasma across the shear layer. Figure 12 shows the mass flux across the center of the shear layer at $x = 0$ as a function of time for cases *A1*, *A2*, *A3*, and *A4*. In all cases, two-fluid simulations exhibit a larger peak mass flux than kinetic simulations, and mass flux values are in better agreement between kinetic and two-fluid simulations for cases with higher magnetization. This trend in mass flux is consistent with the trend observed in the instability growth rates. With the exception of the kinetic simulation of case *A1*, lower magnetization configurations exhibit larger mass flux than higher magnetization configurations. The *A1* kinetic simulation presents an outlier because in the equilibrium state the largest density gradient is offset away from the shear layer.

While the collisionless Kelvin-Helmholtz instability is not a diffusive process, the associated mass flux can be interpreted as an effective one-dimensional diffusion, such that density evolution can be approximately described by

$$\frac{\partial n_s}{\partial t} = \frac{\partial}{\partial x}\left(D\frac{\partial n_s}{\partial x}\right), \tag{50}$$

where D is the diffusion coefficient. Consistent with this approximation and the continuity equation given in Eq. (21), ion particle flux is equivalent to $D\frac{\partial n_i}{\partial x}$. In principle, the diffusion coefficient should encapsulate eddy size and instability growth rate, which captures the effects of shear, perturbation wavelength, density variation, magnetization, and charge separation. For an order-of-magnitude estimate, the diffusion coefficient can be approximated by $D \approx (d/2)^2\omega_I$, where d is the shear layer half-width and ω_I is the instability growth rate. Note that the choice of using $d/2$ as the diffusion scale length was informed by the shifts in the density centroid, shown in Fig. 10. In nondimensional units, $D \approx \frac{1}{4}(\omega_I/\omega_s)$ and $\partial n/\partial x \approx nbd \approx 1$. By these arguments, for the growth rates given in Table II, we

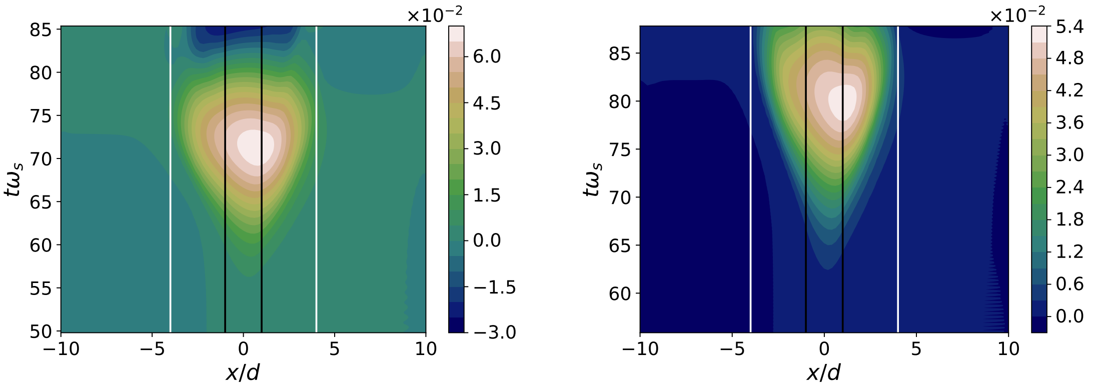

(a) Two-fluid simulation, case *A1*, $\frac{\Omega_p}{\omega_{pp}} = 1$

(b) Two-fluid simulation, case *A2*, $\frac{\Omega_p}{\omega_{pp}} = 2$

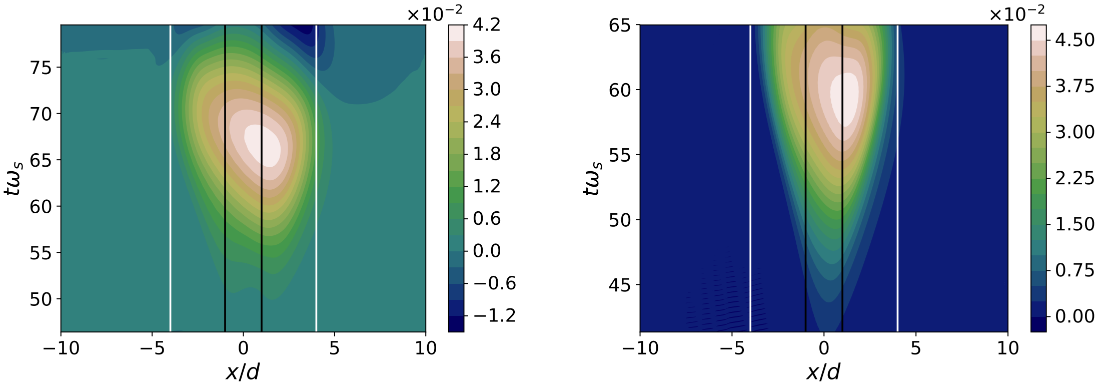

(c) Kinetic simulation, case *A1*, $\frac{\Omega_p}{\omega_{pp}} = 1$

(d) Kinetic simulation, case *A2*, $\frac{\Omega_p}{\omega_{pp}} = 2$

FIG. 11: The nondimensionalized x-directed ion mass flux $\langle M_i n_i u_{ix} \rangle_y / (\omega_s d)$, defined in Eq. (49), plotted as function of position and time for: (a) two-fluid simulation of case *A1* with $\Omega_p/\omega_{pp} = 1$; (b) two-fluid simulation of case *A2* with $\Omega_p/\omega_{pp} = 2$; (c) kinetic simulation of case *A1* with $\Omega_p/\omega_{pp} = 1$; and (d) kinetic simulation of case *A2* with $\Omega_p/\omega_{pp} = 2$. Parameter cases *A1* and *A2* are outlined in Table I. Two-fluid and kinetic simulation results are shown for the nonlinear phase of the KH instability. Black vertical lines at $x/d = \pm 1$ denote the original shear layer width and white vertical lines at $x/d = \pm 4$ denote a region that is four times wider than the original shear layer. The mass flux region widens approximately linearly in time in both kinetic and two-fluid simulations, until mass flux peaks. Mass fluxes from two-fluid and kinetic simulations are in better agreement for case *A2*, which has higher magnetization.

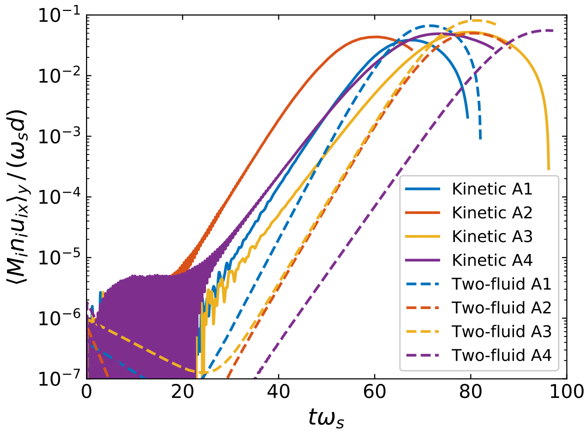

FIG. 12: The x-directed ion mass flux $\langle M_i n_i u_{ix} \rangle_y$, defined in Eq. (49), evaluated at $x = 0$ and plotted as a function of time for parameter cases *A1*, *A2*, *A3*, and *A4* (see Table I). In all cases, two-fluid simulations exhibit a larger peak mass flux than kinetic simulations, and peak values are in better agreement between kinetic and two-fluid simulations for cases with higher magnetization (*A2*,*A4*). This trend is consistent with the trend in growth rate during the linear stage of the KH instability. The mass flux ultimately decreases at a rapid rate, but the time-integrated mass flux remains positive over the time scales simulated, such that plasma exhibits net transport across the shear layer.

would expect a mass flux magnitude of about 10^{-2}, which is consistent with the mass fluxes observed in simulations, shown in Fig. 11 and Fig. 12. As expected, parameter cases with steeper density profiles (cases *A3* and *A4*) result in more plasma being transported across the shear layer.

Kinetic distribution functions, and the degree to which their velocity dependence deviates away from a Maxwellian, provide an indicator of the relative importance of kinetic physics in the collisionless plasmas of interest. The deviation of f_s away from a Maxwellian can be quantified in terms of a relative difference,

$$\delta_{\mathcal{M}} = \frac{\iint |f_s - \mathcal{M}_s| \, dv_x dv_y}{\iint f_s dv_x dv_y}, \tag{51}$$

where $\mathcal{M}_s$ is a Maxwellian distribution function,

$$\mathcal{M}_s = n_s \frac{m_s}{4\pi\sqrt{T_{s1} T_{s2}}} \exp\left(-\frac{m_s (v_x - u_{sx})^2}{4T_{s1}} - \frac{m_s (v_y - u_{sy})^2}{4T_{s2}} \right), \tag{52}$$

whose local density n_s, drift velocity (u_{sx}, u_{sy}), and temperatures (T_{s1}, T_{s2}) are obtained from moments of f_s. For an isotropic Maxwellian $T_{s1} = T_{s2} = \frac{1}{2}(T_{sx} + T_{sy})$, whereas for an

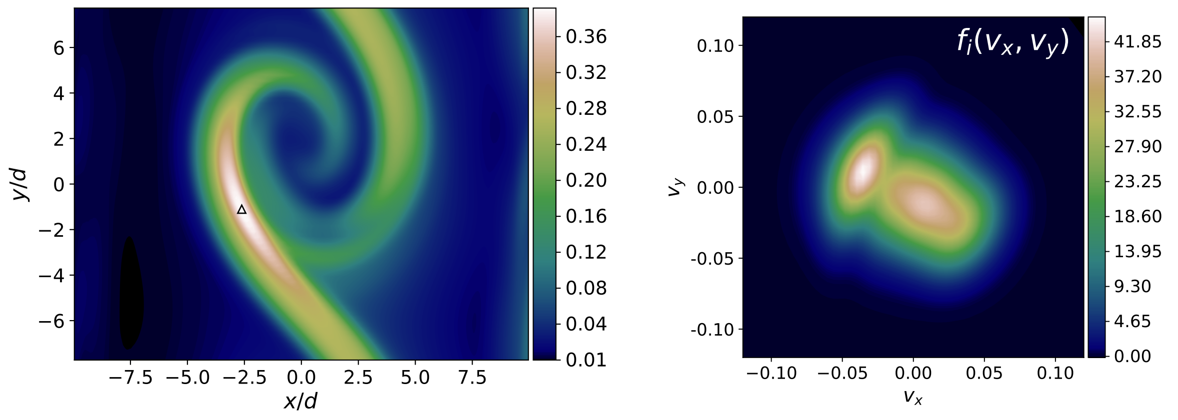

(a) (b)

FIG. 13: (a) Deviation $\delta_{\mathcal{M}}$, defined in Eq. (51), of the kinetic-simulation ion distribution function away from an isotropic Maxwellian for parameter case *A3* (see Table I and Fig. 5) at time $t\omega_s = 85.8$. The maximum deviation is 0.388 and its location is denoted by a black triangle marker. Regions of the domain with velocity shear, density gradients (see Fig. 8(a)), and large Larmor orbits (see Fig. 9) exhibit the largest deviations, indicating that kinetic physics is more important in these regions. (b) The ion distribution function $f_i(v_x, v_y)$ at the point of maximum deviation, plotted on a subset of the velocity domain. The distribution function has two distinct peaks, and is thereby poorly represented by a Maxwellian reconstruction.

anisotropic Maxwellian $T_{s1} = T_{sx}$ and $T_{s2} = T_{sy}$, with T_{sx} and T_{sy} computed from f_s using Eq. (39). For parameter case *A3*, where $\Omega_p/\omega_{pp} = 1$, the maximum deviation of the ion distribution function from an isotropic Maxwellian is 8% at initial time and 39% at time $t\omega_s = 85.8$. As shown in Fig. 13(a) – see also Figs. 8(a) and 9, the largest deviations coincide with regions of the domain with velocity shear, density gradients, and large Larmor orbits. Figure 13(b) shows the ion velocity distribution function $f_i(v_x, v_y)$ plotted at the location of maximum deviation. The distribution function is anisotropic, exhibits two distinct peaks, and an overall tilt in the (v_x, v_y) plane. The latter feature is an indicator of non-zero off-diagonal terms in the pressure tensor. The development of non-Maxwellian features suggests that the nonlinear stage of the KH instability can potentially give rise to subsidiary microinstabilities. The maximum deviation from an anisotropic Maxwellian is 2% at initial time and 38% at time $t\omega_s = 85.8$, indicating that anisotropic pressure does not capture the kinetic physics and higher moments of the distribution function are needed to represent dynamics – as is consistent with previous findings[31]. For parameter case *A4*, where magnetization is $\Omega_p/\omega_{pp} = 2$, the maximum deviation from an isotropic/anisotropic Maxwellian distribution function is only slightly lower – 25% at time $t\omega_s = 83.1$. These deviations grow precipitously during the nonlinear phase of the KH instability evolution, and indicate that the nonlinear state of the plasma is strongly affected by kinetic physics. The large deviations, which can only occur in low-collisionality regimes, also suggest that multi-fluid descriptions based on the first three moments of the distribution function are likely to be inaccurate when it comes to modeling long-time KH instability turbulence. While it is possible that higher-moment multi-fluid descriptions[57–59] can incorporate the observed non-Maxwellian features of the kinetic distribution functions, the applicability of these moment methods is not explored here.

V. CONCLUSION

Hall-MHD linear theory, two-fluid simulations, and kinetic simulations are successfully applied to investigate the properties of KH instabilities in low-beta nonuniform plasmas. The staged approach, using models of increasing fidelity, facilitates the isolated study of different physics and shows how diamagnetic drift, space charge, and finite Larmor motion all modify the evolution of the instability.

Hall-MHD linear theory is applied to characterize KH instabilities in shear layers where the velocity field and the perturbation wave number are transverse to the magnetic field. Unlike previous MHD studies, the analysis admits smooth density variation outside the shear layer and considers finite gradient scale lengths for both velocity and density. An analytic dispersion relation is derived and solved numerically and the growth rate dependence on the density gradient, magnetization, and wavenumber is systematically mapped out. Growth rates are found to be higher for density profiles that decay away from the shear layer. The associated eigenfunctions are also found to be modified from the classical fluid theory and ideal MHD descriptions. When the ratio of ion cyclotron frequency to velocity shear is sufficiently small, i.e. $\Omega_i/\omega_s \lesssim 1$, KH instabilities can couple to drift waves and an associated high wavenumber branch is found to exist, consistent with previous cold fluid[43], large effective Larmor radius MHD[20], and kinetic theory[25,26] analyses.

Two-fluid and kinetic simulations are used to investigate properties of KH instabilities that are beyond the scope of the Hall-MHD description. A finite-element method is used for the two-fluid simulations and a finite-volume discretization is used for Vlasov-Poisson kinetic simulations – both are high-order accurate. Two-fluid simulations capture the complete dynamics of finite-mass electrons and ions and thereby self-consistently capture the physics of space charge and diamagnetic drift. Employing recently developed methods, kinetic Vlasov-Poisson simulations are initialized with self-consistent two-species equilibria that satisfy the steady-state governing equations and fully incorporate finite Larmor radius effects. This technique enables the study of isolated physics in nonuniform plasmas and also enables detailed cross-comparisons with two-fluid simulations. Together, these tools are successfully leveraged to study KH instabilities in nonuniform low-beta plasmas, with significant charge separation, diamagnetic drift, and FLR effects.

Two-fluid and kinetic simulations are conducted for a suite of parameter cases, wherein the density profiles and magnetization are varied. The linear stage of the KH instability evolution in simulations is compared across the different models. In the limit of a uniform quasineutral plasma, two-fluid simulations are found to agree with Hall-MHD predictions. For nonuniform plasmas with significant space charge, the results of two-fluid and kinetic simulations do not agree with Hall-MHD predictions for growth rate and oscillation frequency. In cases where diamagnetic drift constitutes a large fraction of the total equilibrium drift velocity, the errors associated with Hall-MHD predictions for growth rate can be larger than 70%. Two-fluid simulations indicate that the orientation of the diamagnetic drift in the initial equilibrium has a significant effect on the charge distribution, the electric field evolution, and the growth rate. When ion diamagnetic drift opposes the $E \times B$ drift, the growth rates are significantly larger than those predicted by Hall-MHD; whereas when ion diamagnetic drift is aligned with the $E \times B$ drift the growth rates are significantly smaller than those predicted by Hall-MHD. The discrepancy between two-fluid results and Hall-MHD is attributed to the redistribution of charge by polarization drift.

Growth rates obtained from two-fluid simulations and kinetic simulations are in close agreement whenever the shear layer width is at least four Larmor orbits wide. For large Larmor orbits, for example when the ratio of ion Larmor radius to shear layer half-width is $r_{Li}/d = 0.50$, FLR effects lead to diminished growth rates in kinetic simulations as compared to two-fluid simulations. The oscillation frequencies in two-fluid and kinetic simulations match within two percent for all parameter cases.

In the nonlinear phase of the KH instability evolution, two-fluid and kinetic simulation results exhibit similar features – including localized enhancement of diamagnetic drift, heating, and charge accumulation. The fundamental distinction between two-fluid and kinetic results in the nonlinear phase is that FLR effects in kinetic simulations set a minimum bound on the gradient scale lengths, whereas two-fluid simulations – in the absence of viscosity – can develop features that are smaller than the ion Larmor radius. Two-fluid and kinetic simulations of the KH instability are successfully used to study instability-induced mass transport across the shear layer. The transport is characterized in terms of density evolution, mass flux across the shear layer, and a simplified diffusion model. Mass flux is found to be higher for parameter cases with lower magnetization and for parameter cases with steeper density profiles. Two-fluid simulations tend to exhibit larger mass flux. During the nonlinear stage of the instability evolution, ion distribution functions are shown to deviate by more than 30% from Maxwellian reconstructions, particularly in regions with velocity and density gradients and in regions with large gyroradii. In the collisionless plasmas of interest, such deviations point to the importance of kinetic physics in the nonlinear phase of KH instabilities.

Simulations and quantitative comparisons across the different models demonstrate that two-fluid and kinetic effects change the characteristics of the KH instability dramatically. Ion density variation in the shear layer can lead to redistribution of charge via polarization drift, which in turn affects the electric field that drives plasma advection. FLR effects also influence growth rates and can inhibit the development of macroscopic secondary instabilities. The associated growth rates and mass transport properties have important consequences for applications. For the MITL application that motivated this study, the computational results imply that collisionless plasmas created at anode and cathode surfaces can be transported across the magnetic field – contrary to ideal MHD predictions. While the configurations studied here were focused primarily on anode plasmas, simulation results indicate that for the same velocity shear, plasmas near the cathode can be more unstable and thereby subject to more significant mass transport as compared to anode plasmas. The results further suggest that extended MHD models may be inaccurate predictors of cross-field transport in MITL configurations.

There are a number of limitations associated with the present study, which point to future research directions. While time-dependent currents in the electrodes were ignored in the present study, incorporating these currents and the associated magnetic field ramp in simulations would facilitate a more complete description of the MITL configuration. The present study does not explore the effect of multiple unstable modes and secondary instabilities, both of which can affect the nonlinear evolution of the KH instability and the associated mass transport. For example, multiple modes can interact to form larger vortices, the dynamics of which can be affected by the proximity of boundaries. Simulation of longer time scales at higher resolution would also help elucidate whether mass transport continues after multiple roll-ups of the instability. The role of diamagnetic drift and its relative orientation to the equilibrium velocity flow field are shown to be important and warrant further investigation.

ACKNOWLEDGMENTS

G.V.V. would like to thank J. A. F. Hittinger for helpful insights regarding efficient parallel implementation of reflecting-wall boundary conditions in phase space. The kinetic simulations described herein used features of the Chombo library[60] and the PETSc library[61] for parallelization. G.V.V. gratefully acknowledges the support of the Lawrence Postdoctoral Fellowship. This work was performed under the auspices of the U.S. Department of Energy by Lawrence Livermore National Laboratory under Contract DE-AC52-07NA27344 and was supported in part by the LLNL-LDRD Program under Project No. 18-ERD-048. U. Shumlak gratefully acknowledges support as a Faculty Scholar at the Lawrence Livermore National Laboratory. The information, data, or work presented herein was funded in part by the Air Force Office of Scientific Research under Grant No. FA9550-15-1-0271.

This document was prepared as an account of work sponsored by an agency of the United States government. Neither the United States government nor Lawrence Livermore National Security, LLC, nor any of their employees makes any warranty, expressed or implied, or assumes any legal liability or responsibility for the accuracy, completeness, or usefulness of any information, apparatus, product, or process disclosed, or represents that its use would not infringe privately owned rights. Reference herein to any specific commercial product, process, or service by trade name, trademark, manufacturer, or otherwise does not necessarily constitute or imply its endorsement, recommendation, or favoring by the United States government or Lawrence Livermore National Security, LLC. The views and

opinions of authors expressed herein do not necessarily state or reflect those of the United States government or Lawrence Livermore National Security, LLC, and shall not be used for advertising or product endorsement purposes.

The data that support the findings of this study are available from the corresponding author upon reasonable request.

Appendix A: Hall-MHD dispersion relation for KH instability with finite density gradients

Consider the velocity profile in Eq. (13) and density profile in Eq. (14). For the three regions of the domain, Eq. (12) can be expressed as three separate differential equations,

$$0 = \begin{cases} -\hat{u}_{i1x} k_y^2 \left(1 - \frac{a}{\Omega_i k_y}(k_y V - \omega)\right) + a\frac{\partial \hat{u}_{i1x}}{\partial x} + \frac{\partial^2 \hat{u}_{i1x}}{\partial x^2} & x \in [-L, -d] \\ -\hat{u}_{i1x} k_y^2 + \frac{\partial^2 \hat{u}_{i1x}}{\partial x^2} & x \in [-d, d] \\ -\hat{u}_{i1x} k_y^2 \left(1 + \frac{b}{\Omega_i k_y}(k_y V + \omega)\right) + b\frac{\partial \hat{u}_{i1x}}{\partial x} + \frac{\partial^2 \hat{u}_{i1x}}{\partial x^2} & x \in [d, L] \end{cases} \tag{A1}$$

Note that the $\partial \hat{u}_{i1x}/\partial x$ term drops out when piecewise constant density profiles are assumed, e.g. in the analyses presented in Refs. 17 and 20. The general form of the solution $\hat{u}_{i1x}$ that satisfies Eq. (A1) is

$$\hat{u}_{i1x} = \begin{cases} R_a \exp\left(\left\{-\frac{a}{2} - \frac{1}{2}\sqrt{a^2 + 4k_y^2\mathcal{A}}\right\} x\right) + S_a \exp\left(\left\{-\frac{a}{2} + \frac{1}{2}\sqrt{a^2 + 4k_y^2\mathcal{A}}\right\} x\right) & x \in [-L, -d] \\ R_0 e^{k_y x} + S_0 e^{-k_y x} & x \in [-d, d] \\ R_b \exp\left(\left\{-\frac{b}{2} - \frac{1}{2}\sqrt{b^2 + 4k_y^2\mathcal{B}}\right\} x\right) + S_b \exp\left(\left\{-\frac{b}{2} + \frac{1}{2}\sqrt{b^2 + 4k_y^2\mathcal{B}}\right\} x\right) & x \in [d, L] \end{cases} \tag{A2}$$

$$\mathcal{A} = \left(1 - \frac{a}{\Omega_i k_y}(k_y V - \omega)\right) \tag{A3}$$

$$\mathcal{B} = \left(1 + \frac{b}{\Omega_i k_y}(k_y V + \omega)\right) \tag{A4}$$

where R_j and S_j are unknown constant coefficients. Following the approach presented in Refs. 12 and 17, the constant coefficients can be eliminated by applying the following conditions on the solution $\hat{u}_{i1x}$: impermeable wall boundary conditions with $\hat{u}_{i1x} = 0$ at $x = \pm L$; continuity at $x = \pm d$; and the jump condition

$$\left[\frac{-(k_y u_{i0y} - \omega) n_0 \frac{\partial \hat{u}_{i1x}}{\partial x} + n_0 \hat{u}_{i1x} \frac{\partial u_{i0y}}{\partial x} k_y}{1 - \frac{1}{\Omega_i k_y}(k_y u_{i0y} - \omega)\frac{1}{n_0}\frac{\partial n_0}{\partial x}}\right]_{x^-}^{x^+} = 0 \tag{A5}$$

at $x = \pm d$. The jump condition stipulates that the term in the square brackets of Eq. (12) must be continuous at the edges of the shear layer, which ensures that the velocity eigenfunction is continuous. The resulting closed-form nonlocal dispersion relation is

$$
\begin{aligned}
&e^{-4k_y d}\left(\frac{-\frac{a}{2}+\frac{1}{2}\sqrt{a^2+4k_y^2\mathcal{A}}\coth\left(\frac{(L-d)}{2}\sqrt{a^2+4k_y^2\mathcal{A}}\right)-k_y\left(\ \ 1+\frac{V}{d(k_yV-\omega)}\right)\mathcal{A}}{\frac{a}{2}-\frac{1}{2}\sqrt{a^2+4k_y^2\mathcal{A}}\coth\left(\frac{(L-d)}{2}\sqrt{a^2+4k_y^2\mathcal{A}}\right)+k_y\left(-1+\frac{V}{d(k_yV-\omega)}\right)\mathcal{A}}\right)\\
&\qquad=\frac{\left(\ \ \frac{b}{2}+\frac{1}{2}\sqrt{b^2+4k_y^2\mathcal{B}}\coth\left(\frac{(L-d)}{2}\sqrt{b^2+4k_y^2\mathcal{B}}\right)+k_y\left(1-\frac{V}{d(k_yV+\omega)}\right)\mathcal{B}\right)}{\left(-\frac{b}{2}-\frac{1}{2}\sqrt{b^2+4k_y^2\mathcal{B}}\coth\left(\frac{(L-d)}{2}\sqrt{b^2+4k_y^2\mathcal{B}}\right)+k_y\left(1+\frac{V}{d(k_yV+\omega)}\right)\mathcal{B}\right)}.
\end{aligned}
\tag{A6}
$$

In addition to the classical features of the KH instability, Eq. (A6) encapsulates the effects of magnetization, finite density gradients and associated diamagnetic drift, and wall proximity. Given fixed values of $\{d, k_y, L, a, b, V, \Omega_i\}$, Eq. (A6) can be numerically solved for ω.

Appendix B: Hall-MHD dispersion relation for KH instability in limit of classical hydrodynamics

The hydrodynamic dispersion relation for the Kelvin-Helmholtz instability in an infinite uniform-density classical fluid[12] can be obtained by evaluating Eq. (19) in the limit of $\tilde{L} \to \infty, \tilde{\Omega}_i \to \infty, \tilde{b} = 0$, which yields

$$\tilde{\omega} = \pm\frac{1}{2}\sqrt{1 - e^{-4\kappa} - 4\kappa + 4\kappa^2}. \tag{B1}$$

The KH instability grows when the frequency $\tilde{\omega}$ has a positive imaginary component, which happens when $\kappa \in [0, 0.639]$. The maximum nondimensional growth rate is 0.201 and occurs at $\kappa = 0.398$. Allowing for a finite domain size while taking the limits $\tilde{\Omega}_i \to \infty, \tilde{b} = 0$ in Eq. (19), yields the dispersion relation

$$\tilde{\omega} = \pm\frac{1}{2}\sqrt{\frac{\left(e^{2\kappa(1-\tilde{L})} - 1 + 2\kappa\right)^2 - e^{-4\kappa\tilde{L}}\left(e^{2\kappa(\tilde{L}-1)} - 1 - 2\kappa\right)^2}{1 - e^{-4\kappa\tilde{L}}}}, \tag{B2}$$

which is more general than Eq. (B1). As expected, impermeable walls at a finite distance from the shear layer have a stabilizing effect and $\tilde{L} \leq 2$ completely stabilizes the Kelvin-Helmholtz instability.

The dispersion relation for a step density profile, where density is uniform for $x < d$ and zero to the right of the shear layer, can be evaluated by taking the limits $\tilde{L} \to \infty, \tilde{\Omega}_i \to$

$\infty, \tilde{b} \to -\infty$ in Eq. (19), which yields

$$\tilde{\omega} = \frac{1}{4}(1 - e^{-4\kappa}) \mp \frac{1}{4}\sqrt{\Big(e^{-4\kappa} + [3 - 4\kappa]\Big)^2 - 16e^{-4\kappa}}. \tag{B3}$$

For the dispersion relation in Eq. (B3), the frequency has positive imaginary component for $\kappa \in [0, 0.916]$, and the maximum nondimensional growth rate is 0.247 at $\kappa = 0.613$. Thus the configuration is more susceptible to instability when density decreases away from the shear layer. In the limit of $\tilde{L} \to \infty, \tilde{\Omega}_i \to \infty, \tilde{b} \to \infty$, Eq. (19) reduces to the dispersion relation

$$\tilde{\omega} = -\frac{1}{4}\left[1 - e^{-4\kappa}\right] \pm \frac{1}{4}\sqrt{\Big[1 - e^{-4\kappa}\Big]^2 + 8\kappa\Big[e^{-4\kappa} + (2\kappa - 1)\Big]} \tag{B4}$$

wherein the frequency is real-valued and the configuration is stable.

REFERENCES

[1] M. R. Gomez, R. M. Gilgenbach, M. E. Cuneo, C. A. Jennings, R. D. McBride, E. M. Waisman, B. T. Hutsel, W. A. Stygar, D. V. Rose, and Y. Maron, Phys. Rev. Accel. Beams **20**, 010401 (2017), https://doi.org/10.1103/PhysRevAccelBeams.20.010401.

[2] M. H. Hess, B. T. Hutsel, C. A. Jennings, J. P. VanDevender, A. B. Sefkow, M. R. Gomez, P. F. Knapp, G. R. Laity, D. H. Dolan, D. C. Lamppa, K. J. Peterson, W. A. Stygar, and D. B. Sinars, Physics of Plasmas **24**, 013119 (2017), https://doi.org/10.1063/1.4975021.

[3] S. A. Slutz, W. A. Stygar, M. R. Gomez, K. J. Peterson, A. B. Sefkow, D. B. Sinars, R. A. Vesey, E. M. Campbell, and R. Betti, Physics of Plasmas **23**, 022702 (2016), https://doi.org/10.1063/1.4941100.

[4] R. B. Spielman and D. B. Reisman, Matter and Radiation at Extremes **4**, 027402 (2019), https://doi.org/10.1063/1.5089765.

[5] V. V. Ivanov, P. J. Laca, B. S. Bauer, R. Presura, V. I. Sotnikov, A. L. Astanovitskiy, B. Le Galloudec, J. Glassman, and R. A. Wirtz, IEEE Transactions on Plasma Science **32**, 1843 (2004).

[6] Y. L. Bakshaev, A. V. Bartov, P. I. Blinov, A. S. Chernenko, S. A. Dan'ko, Y. G. Kalinin, A. S. Kingsep, V. D. Korolev, V. I. Mizhiritskiĭ, V. P. Smirnov, A. Y. Shashkov, P. V. Sasorov, and S. I. Tkachenko, Plasma Physics Reports **33**, 259 (2007).

[7] T. J. Awe, C. A. Jennings, R. D. McBride, M. E. Cuneo, D. C. Lamppa, M. R. Martin, D. C. Rovang, D. B. Sinars, S. A. Slutz, A. C. Owen, K. Tomlinson, M. R. Gomez, S. B.

Hansen, M. C. Herrmann, M. C. Jones, J. L. McKenney, G. K. Robertson, G. A. Rochau, M. E. Savage, D. G. Schroen, and W. A. Stygar, Physics of Plasmas **21**, 056303 (2014), https://doi.org/10.1063/1.4872331.

[8] D. D. Ryutov, T. J. Awe, S. B. Hansen, R. D. McBride, K. J. Peterson, D. B. Sinars, and S. A. Slutz, AIP Conference Proceedings **1639**, 63 (2014), https://aip.scitation.org/doi/pdf/10.1063/1.4904778.

[9] W. A. Stygar, T. J. Awe, J. E. Bailey, N. L. Bennett, E. W. Breden, E. M. Campbell, R. E. Clark, R. A. Cooper, M. E. Cuneo, J. B. Ennis, D. L. Fehl, T. C. Genoni, M. R. Gomez, G. W. Greiser, F. R. Gruner, M. C. Herrmann, B. T. Hutsel, C. A. Jennings, D. O. Jobe, B. M. Jones, M. C. Jones, P. A. Jones, P. F. Knapp, J. S. Lash, K. R. LeChien, J. J. Leckbee, R. J. Leeper, S. A. Lewis, F. W. Long, D. J. Lucero, E. A. Madrid, M. R. Martin, M. K. Matzen, M. G. Mazarakis, R. D. McBride, G. R. McKee, C. L. Miller, J. K. Moore, C. B. Mostrom, T. D. Mulville, K. J. Peterson, J. L. Porter, D. B. Reisman, G. A. Rochau, G. E. Rochau, D. V. Rose, D. C. Rovang, M. E. Savage, M. E. Sceiford, P. F. Schmit, R. F. Schneider, J. Schwarz, A. B. Sefkow, D. B. Sinars, S. A. Slutz, R. B. Spielman, B. S. Stoltzfus, C. Thoma, R. A. Vesey, P. E. Wakeland, D. R. Welch, M. L. Wisher, and J. R. Woodworth, Phys. Rev. ST Accel. Beams **18**, 110401 (2015).

[10] D. V. Rose, E. A. Madrid, D. R. Welch, R. E. Clark, C. B. Mostrom, W. A. Stygar, and M. E. Cuneo, Phys. Rev. ST Accel. Beams **18**, 030402 (2015).

[11] R. C. Davidson, *Physics of Nonneutral Plasmas* (Imperial College Press London, 2001).

[12] S. Chandrasekhar, *Hydrodynamic and hydromagnetic stability* (Dover, 1981) pp. 483, 487–488.

[13] I. Lerche, Journal of Geophysical Research (1896-1977) **71**, 2365 (1966), https://agupubs.onlinelibrary.wiley.com/doi/pdf/10.1029/JZ071i009p02365.

[14] A. Miura and P. L. Pritchett, Journal of Geophysical Research: Space Physics **87**, 7431 (1982), https://agupubs.onlinelibrary.wiley.com/doi/pdf/10.1029/JA087iA09p07431.

[15] A. Miura, Journal of Geophysical Research: Space Physics **89**, 801 (1984), https://agupubs.onlinelibrary.wiley.com/doi/pdf/10.1029/JA089iA02p00801.

[16] A. Miura, Physics of Plasmas **4**, 2871 (1997), https://doi.org/10.1063/1.872419.

[17] U. Shumlak and N. F. Roderick, Physics of Plasmas **5**, 2384 (1998), https://doi.org/10.1063/1.872913.

[18] Y. Matsumoto and M. Hoshino, Journal of Geophysical Research: Space Physics **111**

(2006), 10.1029/2004JA010988, a05213.

[19] P. Henri, S. S. Cerri, F. Califano, F. Pegoraro, C. Rossi, M. Faganello, O. Šebek, P. M. Trávníček, P. Hellinger, J. T. Frederiksen, A. Nordlund, S. Markidis, R. Keppens, and G. Lapenta, Physics of Plasmas **20**, 102118 (2013), https://doi.org/10.1063/1.4826214.

[20] E. N. Opp and A. B. Hassam, Physics of Fluids B: Plasma Physics **3**, 885 (1991), https://doi.org/10.1063/1.859845.

[21] J. D. Huba, Geophysical Research Letters **23**, 2907 (1996), https://agupubs.onlinelibrary.wiley.com/doi/pdf/10.1029/96GL02767.

[22] T. K. M. Nakamura, D. Hayashi, M. Fujimoto, and I. Shinohara, Phys. Rev. Lett. **92**, 145001 (2004).

[23] V. A. Thomas and D. Winske, Journal of Geophysical Research: Space Physics **98**, 11425 (1993), https://doi.org/10.1029/93JA00604.

[24] M. Fujimoto and T. Terasawa, Journal of Geophysical Research: Space Physics **99**, 8601 (1994), https://agupubs.onlinelibrary.wiley.com/doi/pdf/10.1029/93JA02722.

[25] G. Ganguli, Y. C. Lee, and P. J. Palmadesso, The Physics of Fluids **31**, 823 (1988), http://aip.scitation.org/doi/pdf/10.1063/1.866818.

[26] D. S. Lemons, D. Winske, and S. P. Gary, Journal of Geophysical Research: Space Physics **97**, 19381 (1992), https://agupubs.onlinelibrary.wiley.com/doi/pdf/10.1029/92JA01735.

[27] G. Ganguli, Physics of Plasmas **4**, 1544 (1997), https://doi.org/10.1063/1.872285.

[28] T. Umeda, J.-I. Miwa, Y. Matsumoto, T. K. M. Nakamura, K. Togano, K. Fukazawa, and I. Shinohara, Physics of Plasmas **17**, 052311 (2010), http://dx.doi.org/10.1063/1.3422547.

[29] T. Umeda, S. Ueno, and T. K. M. Nakamura, Plasma Physics and Controlled Fusion **56**, 075006 (2014).

[30] T. K. M. Nakamura, H. Hasegawa, and I. Shinohara, Physics of Plasmas **17**, 042119 (2010), https://doi.org/10.1063/1.3385445.

[31] T. Umeda, Physics of Plasmas **27**, 032112 (2020), https://doi.org/10.1063/1.5139442.

[32] W. Horton, T. Tajima, and T. Kamimura, The Physics of Fluids **30**, 3485 (1987), https://aip.scitation.org/doi/pdf/10.1063/1.866429.

[33] M. Faganello and F. Califano, Journal of Plasma Physics **83**, 535830601 (2017).

[34] F. Malara, O. Pezzi, and F. Valentini, Phys. Rev. E **97**, 053212 (2018), https://doi.org/10.1103/PhysRevE.97.053212.

[35] G. V. Vogman, J. H. Hammer, and W. A. Farmer, Physics of Plasmas **26**, 042119 (2019),

https://doi.org/10.1063/1.5089465.

[36]B. B. Kadomtsev, Soviet Physics JETP **18**, 847 (1964).

[37]A. B. Mikhailovskii, *Electromagnetic Instabilities in an Inhomogeneous Plasma*, Vol. 1 (CRC Press, 1992) p. xvii.

[38]M. Yamada, S. Seiler, H. W. Hendel, and H. Ikezi, The Physics of Fluids **20**, 450 (1977), https://aip.scitation.org/doi/pdf/10.1063/1.861882.

[39]J. D. Huba, Physics of Fluids B: Plasma Physics **3**, 3217 (1991), https://doi.org/10.1063/1.859752.

[40]N. Lindgren, A. B. Langdon, and C. Birdsall, Physics of Fluids (1958-1988) **19**, 1026 (1976).

[41]F. F. Chen, The Physics of Fluids **7**, 949 (1964), https://aip.scitation.org/doi/pdf/10.1063/1.1711341.

[42]W. A. Farmer, C. L. Ellison, and J. H. Hammer, Physics of Plasmas **26**, 072120 (2019), https://doi.org/10.1063/1.5094349.

[43]O. Buneman, R. H. Levy, and L. M. Linson, Journal of Applied Physics **37**, 3203 (1966), https://doi.org/10.1063/1.1703185.

[44]U. Shumlak, R. Lilly, N. Reddell, E. Sousa, and B. Srinivasan, Computer Physics Communications **182**, 1767 (2011).

[45]A. Ho, I. A. M. Datta, and U. Shumlak, Frontiers in Physics **6**, 105 (2018).

[46]U. Shumlak and J. Loverich, Journal of Computational Physics **187**, 620 (2003).

[47]J. Loverich and U. Shumlak, Computer Physics Communications **169**, 251 (2005).

[48]J. Loverich, A. Hakim, and U. Shumlak, Communications in Computational Physics **9**, 240 (2011).

[49]S. Gottlieb, C.-W. Shu, and E. Tadmor, SIAM Review **43**, 89 (2001), https://doi.org/10.1137/S003614450036757X.

[50]G. V. Vogman, P. Colella, and U. Shumlak, Journal of Computational Physics **277**, 101 (2014), http://dx.doi.org/10.1016/j.jcp.2014.08.014.

[51]G. V. Vogman, *Fourth-order conservative Vlasov-Maxwell solver for Cartesian and cylindrical phase space coordinates*, Ph.D. thesis, University of California Berkeley (2016).

[52]G. V. Vogman, U. Shumlak, and P. Colella, Journal of Computational Physics **373**, 877 (2018), https://doi.org/10.1016/j.jcp.2018.07.029.

[53]D. Cai, L. R. O. Storey, and T. Neubert, Physics of Fluids B: Plasma Physics **2**, 75 (1990),

https://doi.org/10.1063/1.859541.

[54] B. B. Kadomtsev, *Plasma Turbulence* (Academic Press Inc., 1965).

[55] D. A. Knoll and L. Chacón, Phys. Rev. Lett. **88**, 215003 (2002).

[56] L. Chacón, D. Knoll, and J. Finn, Physics Letters A **308**, 187 (2003).

[57] T. Chust and G. Belmont, Physics of Plasmas **13**, 012506 (2006), https://doi.org/10.1063/1.2138568.

[58] S. T. Miller and U. Shumlak, Physics of Plasmas **23**, 082303 (2016), https://doi.org/10.1063/1.4960041.

[59] J. Ng, A. Hakim, and A. Bhattacharjee, Physics of Plasmas **25**, 082113 (2018), https://doi.org/10.1063/1.5041758.

[60] M. Adams, P. Colella, D. Graves, J. Johnson, H. Johansen, N. Keen, T. Ligocki, D. Martin, P. McCorquodale, D. Modiano, P. Schwartz, T. Sternberg, and B. Van Straalen, "Chombo software package for AMR applications – design document," Tech. Rep. LBNL-6616E (Lawrence Berkeley National Laboratory, 2015).

[61] S. Balay, S. Abhyankar, M. F. Adams, J. Brown, P. Brune, K. Buschelman, L. Dalcin, V. Eijkhout, W. D. Gropp, D. Kaushik, M. G. Knepley, L. C. McInnes, K. Rupp, B. F. S. S. Zampini, and H. Zhang, "PETSc users manual," Tech. Rep. ANL-95/11 - Revision 3.6 (Argonne National Laboratory, 2015).